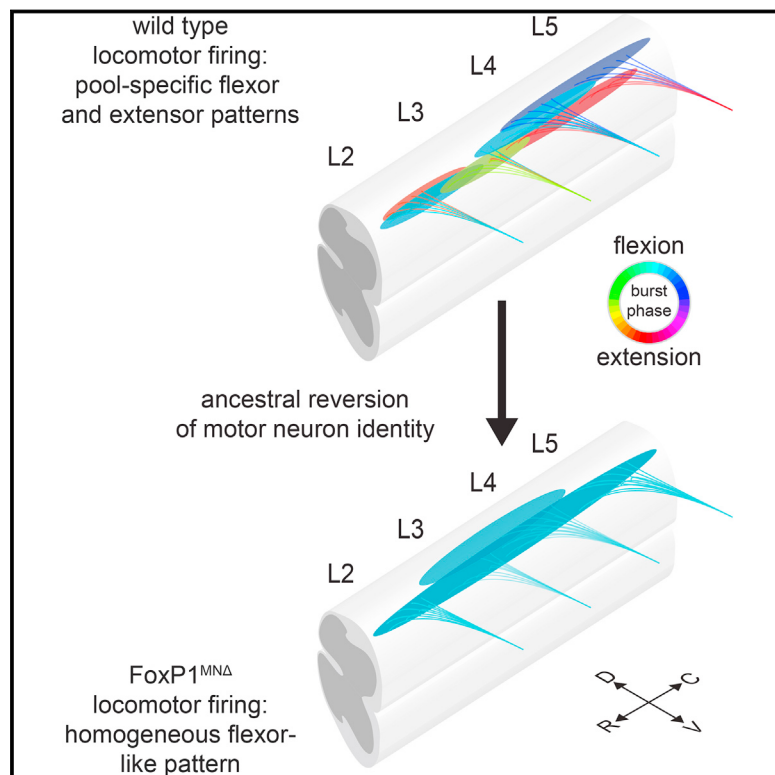


Primacy of Flexor Locomotor Pattern Revealed by Ancestral Reversion of Motor Neuron Identity

Graphical Abstract



Authors

Timothy A. Machado, Eftychios Pnevmatikakis, Liam Paninski, Thomas M. Jessell, Andrew Miri

Correspondence

tam2138@columbia.edu (T.A.M.), tmj1@columbia.edu (T.M.J.)

In Brief

Measurements of locomotor firing in hundreds of limb-innervating motor neurons reveal organization of circuits driving flexor and extensor muscles. Ancestral reversion of motor neuron identity converts all firing patterns to flexor like, indicating that motor neuron identity contributes to the wiring of locomotor circuits and favors the evolutionary primacy of flexor pattern generation.

Highlights

- Motor neurons that innervate synergist muscles show synchronous locomotor firing
- Flexor motor neurons activate in a sequence that matches target muscle positioning
- Motor neuron columnar identity specifies locomotor firing pattern
- Ancestral reversion of motor neuron identity reveals the primacy of flexor pattern



Primacy of Flexor Locomotor Pattern Revealed by Ancestral Reversion of Motor Neuron Identity

Timothy A. Machado,^{1,2,*} Eftychios Pnevmatikakis,^{2,3} Liam Paninski,² Thomas M. Jessell,^{1,*} and Andrew Miri¹

¹Departments of Neuroscience and Biochemistry and Molecular Biophysics, Howard Hughes Medical Institute, Kavli Institute of Brain Science, Columbia University, New York, NY 10032, USA

²Department of Statistics, Center for Theoretical Neuroscience and Grossman Center for the Statistics of Mind, Columbia University, New York, NY 10027, USA

³Simons Center for Data Analysis, Simons Foundation, New York, NY 10010, USA

*Correspondence: tam2138@columbia.edu (T.A.M.), tmj1@columbia.edu (T.M.J.)

<http://dx.doi.org/10.1016/j.cell.2015.06.036>

SUMMARY

Spinal circuits can generate locomotor output in the absence of sensory or descending input, but the principles of locomotor circuit organization remain unclear. We sought insight into these principles by considering the elaboration of locomotor circuits across evolution. The identity of limb-innervating motor neurons was reverted to a state resembling that of motor neurons that direct undulatory swimming in primitive aquatic vertebrates, permitting assessment of the role of motor neuron identity in determining locomotor pattern. Two-photon imaging was coupled with spike inference to measure locomotor firing in hundreds of motor neurons in isolated mouse spinal cords. In wild-type preparations, we observed sequential recruitment of motor neurons innervating flexor muscles controlling progressively more distal joints. Strikingly, after reversion of motor neuron identity, virtually all firing patterns became distinctly flexor like. Our findings show that motor neuron identity directs locomotor circuit wiring and indicate the evolutionary primacy of flexor pattern generation.

INTRODUCTION

The mammalian nervous system is charged with the task of moving limbs—a challenge met through the construction of spinal circuits that coordinate interwoven patterns of muscle activity. Motor patterns reflect the activation of selected pools of motor neurons which, in turn, are driven by descending commands, peripheral feedback, and input from spinal premotor interneurons. Many studies have invoked the idea that local spinal circuits alone can sustain motor neuron burst firing in patterns that resemble the rhythmic alternation of antagonist muscles during locomotion (Grillner and Zangerer, 1975; Kiehn and Kjaerulff, 1996; Kudo and Yamada, 1987). Yet the basic rules of spinal circuit organization that govern the rhythmicity and alternation of locomotor output remain unclear.

Attempts to delineate the spinal circuitry of mammalian locomotion have focused largely on connections among interneurons with presumed roles in pattern generation. One long-held view proposes that the premotor circuits that direct the alternation of antagonist flexor and extensor muscles exhibit an interdependence achieved through reciprocal interneuronal connections (Brown, 1914; McCrea and Rybak, 2008; Talpalar et al., 2011; Zhang et al., 2014). But the obligate role of reciprocal connectivity has been called into question by observations that rhythmic flexor or extensor motor output can, under rare circumstances, occur without activation of their antagonist pair (Burke et al., 2001; Pearson and Duyens, 1976; Zhong et al., 2012). Because spinal interneurons should be capable of distinguishing the identity of flexor and extensor motor neurons, we reasoned that insight into the organization of locomotor circuits might emerge from a focus on the recognition and selection of motor pools by premotor interneurons, rather than on the intricacies of interneuron interconnectivity.

The genetic identities, muscle targets, and functional specialization of motor neurons have diversified greatly during vertebrate evolution, suggesting the utility of addressing the influence of motor neuron identity on locomotor pattern. Within this broad evolutionary context, certain physiological findings are consistent with the idea that mammalian flexor networks evolved by co-opting a core axial motor circuit responsible for swimming in ancestral aquatic vertebrates. In primitive vertebrates, body undulations during swimming reflect the sequential recruitment of motor neurons innervating segmentally arrayed axial muscles (Grillner and Wallén, 2002). A similar wave-like sequence of motor neuron activation is evident from ventral root recordings at thoracic levels in the isolated rodent spinal cord during locomotor-like activity (Beliez et al., 2015; Falgairolle and Cazalets, 2007). This thoracic wave reflects the firing of median (MMC) and hypaxial (HMC) motor column neurons that innervate trunk and body wall muscles—the mammalian derivatives of primitive axial muscles (Kusakabe and Kuratani, 2005). Intriguingly, the firing of lumbar level flexor motor neurons represents a caudal continuation of the thoracic activity wave, whereas extensor motor neurons burst in antiphase (Falgairolle and Cazalets, 2007). This continuity of thoracic and flexor firing may reflect the reappropriation of axial circuits for flexor pattern generation and thus the evolutionary primacy of the flexor system. The idea that the basic organization of modern flexor circuits predates the

emergence of extensor circuits implies that the generation of flexor-like patterns may not require interdependence between flexor and extensor circuits.

To explore the concept of flexor primacy and examine how motor neuron identity shapes the formation of locomotor circuits, we constructed cellular resolution maps of locomotor pattern in the absence of descending commands and sensory feedback. Two-photon imaging and spike inference were combined to measure the firing of hundreds of target-defined motor neurons in an isolated neonatal mouse spinal cord preparation induced to locomotor-like activity (Bonnot et al., 2002; Kwan et al., 2009). Our analysis revealed that motor pools innervating muscles with synergistic functions fire synchronously and that flexor pools are activated in a ventral-to-dorsal sequence that matches the proximodistal order of their target muscles along the limb.

This characterization of the wild-type pattern of motor neuron activation served as a reference in analyzing how the ancestral reversion of lumbar motor neuron identity modifies locomotor pattern. The concept of flexor primacy suggests that reversion of lateral motor column (LMC) neurons to an ancestral-like state will lead to their recruitment of flexor-defining premotor inputs. To address this possibility, we used genetic inactivation of the FoxP1 transcription factor to convert limb-innervating motor neurons to an HMC-like ground state (Dasen et al., 2008; Kusakabe and Kuratani, 2005; Russo et al., 2008). In *FoxP1* mutant preparations, we find that virtually all limb-innervating motor neurons—those innervating extensor as well as flexor limb muscles—are activated with the precise temporal features of flexor motor neurons. These observations show that the subtype identity of motor neurons profoundly influences the pattern of motor output. They also lend credence to the idea that a flexor-like motor pattern emerged during vertebrate evolution without reliance on an opponent extensor circuit.

RESULTS

Motor Neuron Firing Phase at Cellular Resolution

We monitored Ca^{2+} -sensitive fluorescence in hindlimb-innervating motor neurons in isolated postnatal day 2 to 5 mouse spinal cord preparations induced to a state of locomotor-like activity by glutamate and monoamine receptor agonists (5 μM NMDA, 10 μM 5-HT, 50 μM DA) (Figures 1A–1D; Kudo and Yamada, 1987). Motor neuron expression of the Ca^{2+} indicator GCaMP3 was achieved by crossing mice carrying a conditional ROSA-CAG-*Isl*-GCaMP3 allele (Zariwala et al., 2012) with *Olig2::Cre* or *ChAT::Cre* motor neuron driver lines (Lowell et al., 2006; Sürmeli et al., 2011). Prior to imaging, groups of synergist muscles were injected with Alexa 555- or 647-conjugated cholera toxin B subunit (CTB) to identify motor neurons by their targets. Two-photon microscopy was used to acquire 90 s GCaMP3 fluorescence image sequences from 22 to 64 sagittal imaging fields ($512 \mu\text{m} \times 512 \mu\text{m}$) that collectively spanned lumbar segments L2 to L6. Concurrent recordings of rhythmic activity from ventral roots L1 or L2 provided a reference signal for measuring motor neuron burst firing phase, with the locomotor cycle defined as the interval between peaks of L1/2 activity (peaks = 0°). Recordings from L4 or L5 (Figure 1B) and contralat-

eral L1/L2 roots (data not shown) established that the alternating burst firing characteristic of locomotor activity was evident in each preparation.

We aimed to define firing features through the analysis of Ca^{2+} -sensitive fluorescence from motor neuron cell bodies, but slow Ca^{2+} extrusion and noise in fluorescence measurements obscure prominent burst features such as duration and the phase of peak firing (Figure S1A; Helmchen and Tank, 2005). To overcome this problem, we used an improved, model-based statistical algorithm that infers the spike train most likely to underlie a somatic fluorescence time series (Figures S1B and S1C; Pnevmatikakis et al., 2014). This algorithm fits fluorescence data using a model of spike-related fluorescence fluctuations that assumes each action potential results in a fluorescence transient with instantaneous rise and exponential decay, in the added presence of Gaussian noise. For each somatic fluorescence time series, the algorithm yields a relative estimate of the number of spikes that occurred during each imaging frame. These normalized spike counts were assembled into histograms that display the rhythmic burst firing of each motor neuron during the image sequence (black bars in Figure 1E). To quantify burst timing, the mean phase of each burst was calculated, and the median of these values was defined as a neuron's phase tuning (Figures 1D and 1F).

The validity of such quantification depends on the ability of the spike inference model to capture the relationship between firing and fluorescence. The model was calibrated and its applicability evaluated by exploiting the fact that motor neurons activated antidromically by ventral root stimulation fire in patterns that follow stimulus timing (Figures S2A–S2E; Bonnot et al., 2005). For each experimental preparation, a single fluorescence transient decay time constant was computed using fluorescence measurements obtained during patterned antidromic stimulation that mimicked locomotor-like rhythmic burst firing. Use of these preparation-specific time constant values corrected for decay time variation between preparations (Figures S2F–S2H). In addition, analysis of somatic fluorescence acquired during antidromic activation indicated that models incorporating the saturation of indicator binding do not provide a more accurate prediction of spiking (Figures S1D and S1E), justifying use of a model that does not take saturation into account.

To assess the accuracy of spike inference, we examined phase tuning estimates for individual motor neurons during antidromic stimulation (Figure S2D). Tuning measurements derived from spike inference were nearly identical to values computed directly from antidromic stimuli (mean difference \pm SD = $-2.0 \pm 10.7^\circ$, n = 367 neurons; Figures S2G and S2H). Thus, spike inference permits accurate estimation of motor neuron phase tuning.

In each spinal cord preparation, motor neurons are spread across many imaging fields, and as such, neuron-by-neuron comparisons of phase tuning require that values be stable over time. To assess tuning stability, we imaged a subset of fields in individual preparations at time points separated by 20 to 220 min. Importantly, even if tuning is stable, errors intrinsic to the measurement of burst phase from inferred spiking will result in variation in tuning estimates between time points. We estimated this error from the tuning of motor neurons imaged during

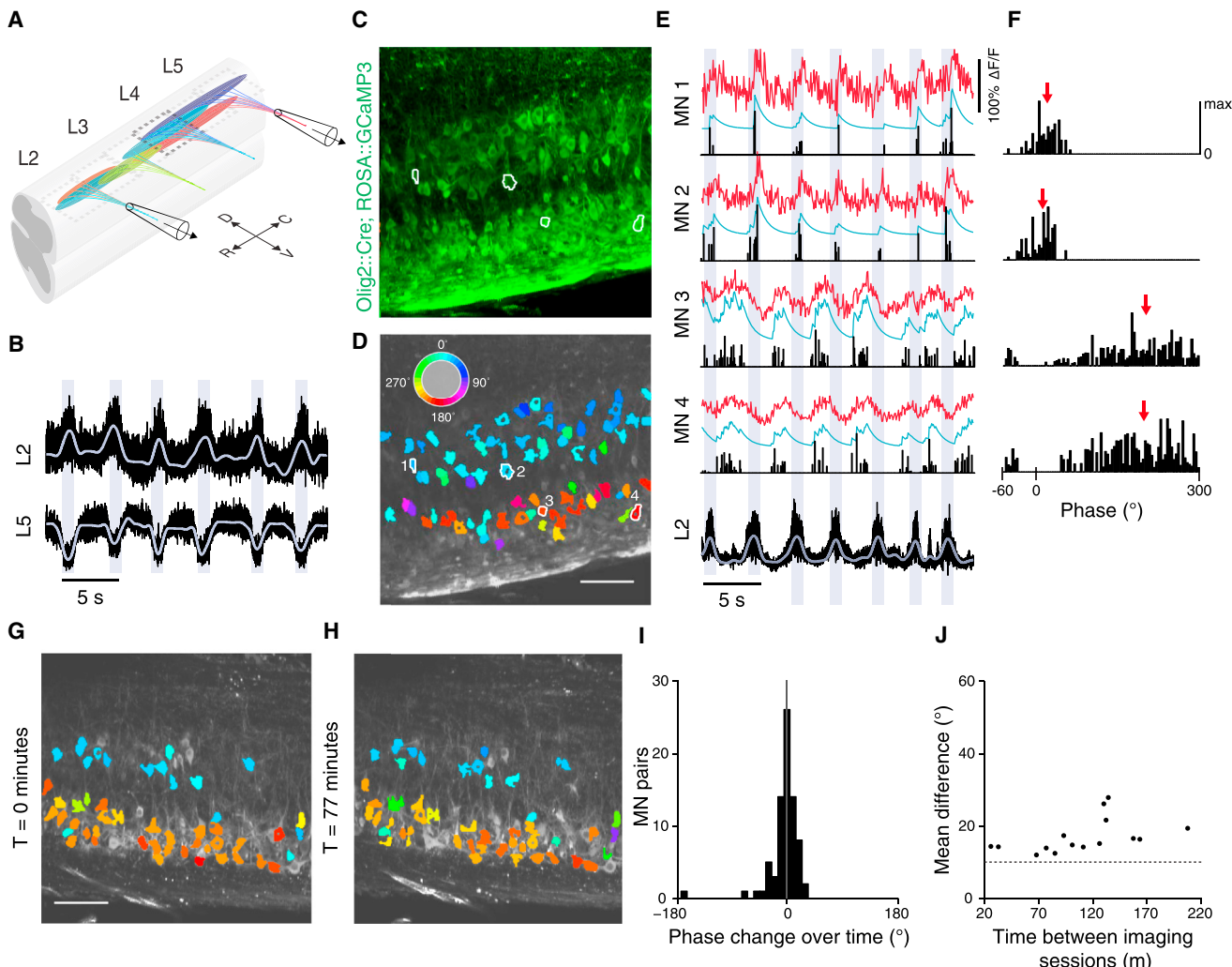


Figure 1. Measuring Locomotor Firing from Motor Neuron Ca^{2+} -Sensitive Fluorescence

(A) Schematic of the neonatal whole-cord preparation used for imaging. LMC motor pools and their corresponding roots are shown in color.
 (B) Ventral root recordings (DC to 1 kHz) obtained from L2 and L5 roots during agonist-induced locomotor firing.
 (C) Single imaging field containing GCaMP3-expressing motor neurons (green).
 (D) ROIs for motor neurons in (C) colored according to phase tuning. Scale bars in (D) and (G) are 100 μm . Phase color map is inset.
 (E) Fluorescence time courses (red) for four motor neurons from (C and D) along with spike-induced fluorescence model fit (cyan) and inferred spiking (black bars).
 (F) Inferred spike counts from a full 90 s image sequence are plotted across the locomotor cycle (L2 root signal peaks = 0°) for the four motor neurons in (E), with the phase tuning of each neuron indicated (red arrows). Bin widths are 4°. Max height indicates the maximum per bin spike count.
 (G and H) Phase tuning for motor neurons measured twice during an experiment (0 and 77 min later) to assess phase tuning stability.
 (I) Distribution of tuning changes for all motor neurons (76 pairs) imaged in the preparation shown in (G) and (H). Mean change = -2°, SD = 21°.
 (J) Mean tuning difference versus the interval between measurements for 15 mice (1,714 neurons). Dotted line indicates predicted mean difference assuming stable phase tuning.

See also Figures S1 and S2.

antidromic activation, when all neurons fire in synchrony. The distribution of these tuning values indicated that two separate estimates of the same underlying tuning would differ on average by 10.1°. In comparison, temporally separated estimates of motor neuron firing during agonist-induced locomotor-like activity exhibited a similar difference of only 12.0° on average ($n = 1,714$ neuron pairs; Figures 1G–1J). Moreover, the slope of a linear regression fit indicated an incremental deviation of tuning values of only 2.8° per hr. Together, these findings establish that

the phase tuning of LMC motor neurons in individual preparations is relatively stable over the duration of data collection. Thus, phase tuning estimates are both accurate and stable, enabling assessment of the relative tuning of motor neurons that innervate different limb muscles.

Synergy Group-Specific Locomotor Firing

Pools of motor neurons that innervate muscles with similar functions at an individual joint form functional synergy groups and are

clustered within the spinal cord (McHanwell and Biscoe, 1981; Vanderhorst and Holstege, 1997). To examine whether the phase tuning of motor neurons segregates with synergy group identity, we analyzed between 400 and 1,400 limb-innervating motor neurons in each preparation that exhibited phasic firing (mean = 818 motor neurons; Figures S3A–S3C; Berens, 2009). Spatial tuning maps were constructed, with the position of each motor neuron in three-dimensional space noted in a color that indicates its tuning (Figures 2A–2J and Movies S1 and S2). These maps revealed numerous motor neurons with tuning close to the reference ventral root activity peak ($L1/2 = 0^\circ$), and many others with near-antiphase ($\sim 180^\circ$) tuning, at each lumbar segmental level (Figures S4A–S4D). Motor neurons with similar tuning were arranged in rostrocaudally elongated clusters that formed clear boundaries with other neuronal clusters of distinct tuning. These coherent clusters were similar in shape and extent to motor pool synergy groups, suggesting a direct correspondence between firing phase and synergy group identity. These findings contrast with prior reports of a wave-like sequence of motor neuron activation along the rostrocaudal axis of the LMC that transgresses synergy group boundaries (O'Donovan et al., 2008).

To probe further the correspondence between identity and firing phase, we measured the phase tuning of motor neurons that had been assigned to particular synergy groups (Figures 2K–2N). CTB was injected into four muscle groups: the intrinsic foot (IF; toe flexors), anterior crural (AC; ankle flexors), quadriceps (Q; knee extensor/hip flexor), and gluteal (G; hip extensor/flexor) muscles, and the tuning of retrogradely labeled motor neurons was measured. Identified IF and AC motor neuron populations exhibited unimodal tuning distributions, whereas Q and G motor neuron populations displayed bimodal distributions (Figures S4E–S4H). Among Q motor neurons, the more lateral, presumptive rectus femoris (RF) motor neurons were tuned near 0° , whereas the more medial, presumptive vastus (V) motor neurons were tuned close to 180° (De Marco Garcia and Jessell, 2008; Vanderhorst and Holstege, 1997; Figure S4G). Similarly, for G motor neurons, a more rostral, presumptive tensor fasciae latae (TFL) cluster was tuned near 0° , whereas a caudal cluster containing the three remaining gluteal motor pools (GM) was tuned around 180° (Figure S4H). These results are consistent with functional definitions of RF and TFL as hip flexors and V and GM muscles as knee and hip extensors, respectively (Platzner, 2004). The alignment of six synergy groups with phasically homogeneous clusters in tuning maps supports the view that phase tuning is organized in register with synergy group identity.

If locomotor firing is synergy group specific, then cycle-by-cycle covariation in the phase of burst firing might be stronger within than between groups. To test this possibility, we evaluated burst phase covariation using a synchrony index that reflects across-cycle consistency in phase differences between pairs of motor neurons (Figures 3A–3C; Mormann et al., 2000). We observed higher synchrony among motor neurons assigned to the same synergy group by CTB labeling (Figure 3D, mean index \pm SEM = 0.51 ± 0.007 , n = 517 pairs; $p < 10^{-10}$, Wilcoxon test) and lower synchrony among motor neurons assigned to different synergy groups (Figure 3D, mean index \pm SEM = 0.33 ± 0.026 , n = 68 pairs; $p = 4.2 \times 10^{-7}$, Wilcoxon test;

comparing with synergist pairs, $p = 4.4 \times 10^{-10}$, Wilcoxon test; $p = 4.7 \times 10^{-6}$ after controlling for differences in proximity). Thus, synergist motor neurons are preferentially synchronized.

We also assessed the degree of phase synchrony for synergist motor neuron pairs as a function of their separation. Synchrony indices did not vary significantly with proximity along the rostro-caudal axis (Spearman correlation [ρ] = -0.07 , $p = 0.12$; Figure 3E). In contrast, we detected a shallow proximity dependence along the dorsoventral axis ($\rho = -0.09$, $p = 0.04$; Figure 3F), which may reflect slightly elevated synchrony within the motor pools that comprise each synergy group. Nevertheless, as a whole, these findings indicate that the major determinant of synchrony in motor neuron burst phase is synergy group membership.

Positional Order and the Sequential Activation of Flexor Synergy Groups

Walking is characterized by the sequential activation of limb muscles, with a precision in recruitment that reflects their biomechanical function (Rossignol, 1996). To examine the degree to which the order of muscle recruitment can be imposed by local spinal circuits, we characterized the sequential activation of flexor synergy groups innervating different limb joints. Normalized spike histograms were used to derive an average firing rate across the locomotor cycle for individual motor neurons within defined synergy groups (Figures 4A–4F, bottom; Figures 2K–2N). Because Q and G motor neurons display bimodal tuning, we used k-means clustering ($k = 2$) to separate the cycle-averaged firing rates of both groups, yielding distinct RF and V pools at different mediolateral positions within the Q population, and rostrocaudally distinct TFL and GM pools within the G population (Figures S4G and S4H). Mean cycle-averaged firing rates for individual synergy groups showed that the phase of peak firing and burst duration were consistent across preparations (Figures 4A–4F, colored traces in top panels).

Strikingly, we found a tight correspondence between the dorsoventral position of synergy groups and the onset of their activation, assessed here as the time at which firing rates attained 50% of their eventual maxima (Figures 4G and 4H). The mean firing of the ventral-most motor neurons innervating the hip flexor TFL had an onset at a cycle phase of $-43.8 \pm 20.9^\circ$ (median \pm SE of median, n = 34 neurons). The firing of more dorsally positioned motor neurons innervating RF, a hip flexor with a more distal origin and insertion than TFL, had an onset at $-33.0 \pm 4.4^\circ$ (n = 38). The firing of still more dorsally positioned motor neurons innervating ankle flexor AC muscles had an onset at $-13.2 \pm 2.2^\circ$ (n = 106). Finally, the dorsal-most motor neurons, which innervate toe flexor IF muscles, had an onset at $19.2 \pm 2.6^\circ$ (n = 72). The correlations of both burst onset phase and peak firing phase with position were strong (onset: $\rho = 0.70$, $p < 10^{-10}$; peak: $\rho = 0.69$, $p < 10^{-10}$, Figures 4G and 4H). Thus local spinal circuits appear able to impose a motor neuron activation order that follows their settling positions and thus the proximodistal order of their target muscles.

Flexor-like Locomotor Firing after Reversion of Motor Neuron Identity

Are locomotor firing patterns modified by reverting motor neuron columnar identity to an ancestral-like state? To test this

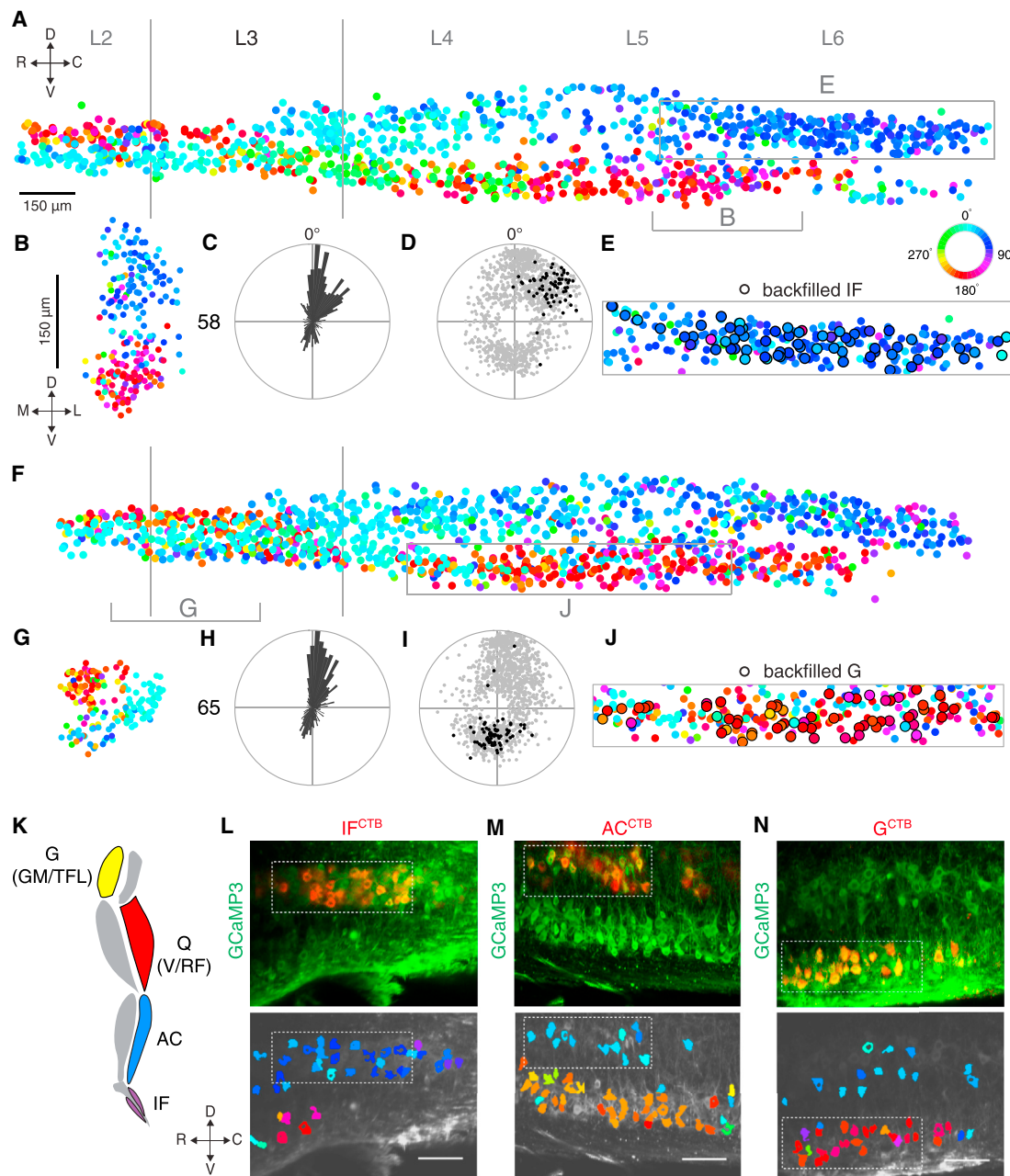


Figure 2. Spatial Maps of Motor Neuron Phase Tuning across the LMC

(A and F) Maps showing phase tuning of motor neurons within the spinal cord as viewed from the lateral side. Data were obtained from two different preparations (1,177 neurons in [A] and 1,264 neurons in [F]). Boundaries of the antidromically activated segment are indicated by vertical lines. Labels of other segments were drawn assuming equal segment widths.

(B and G) Transverse projections for the rostrocaudal extent indicated in (A) and (F), respectively.

(C and H) Polar histogram showing the phase tuning of neurons mapped in (A) and (F), respectively. The maximal number of neurons within a single bin is shown to the left of each histogram.

(D and I) Polar plot indicating the phase tuning of all motor neurons mapped in (A) and (F), respectively, in gray. CTB-labeled intrinsic foot (IF; D) and gluteal (G; I) motor neurons are shown in black. The radial position of each point represents the circular spread of its phase tuning.

(E and J) Magnification of the boxed areas in (A) and (F), respectively, shows CTB-labeled neurons in detail.

(K) Schematic leg showing the position of all muscle groups characterized using CTB.

(L) Top: sagittal spinal cord section showing the position of IF neurons (red). Bottom: ROIs for motor neurons with significantly phasic activity colored according to phase tuning using the same color scale as (A). Dotted line denotes a region containing CTB-labeled IF motor neurons.

(M and N) Same format as (L) but for two additional muscle groups: (M) anterior crural (AC), (N) gluteal (G). Scale bar in each image is 100 μm.

See also Figures S3 and S4 and Movies S1 and S2.

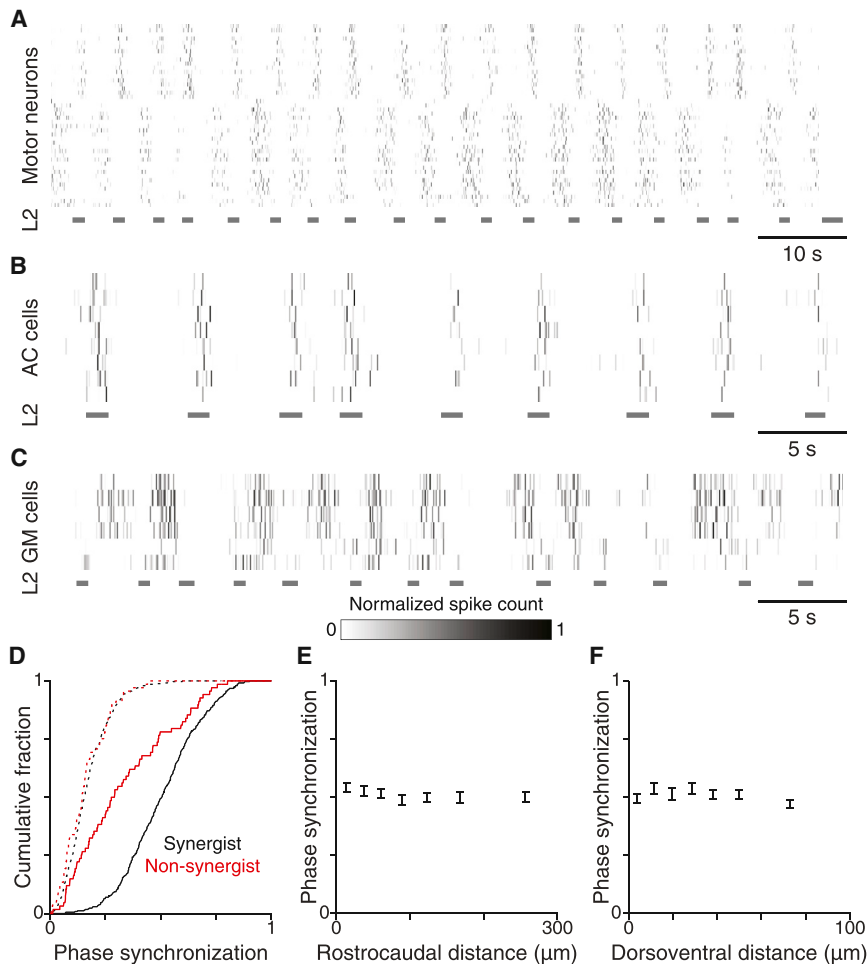


Figure 3. Assessment of Synchrony in Locomotor Firing within and across Synergy Groups

(A) Normalized spike histograms of 44 simultaneously imaged motor neurons, illustrating synchronized firing across locomotor cycles. The normalized spike count computed for each imaging frame is indicated by a grayscale tick mark horizontally spanning the frame duration (67 ms). Wide gray bars at bottom denote periods of elevated L2 ventral root activity. For panels (A) to (C), the normalized spike count for each imaging frame is indicated in grayscale according to the scale bar below (C).

(B) Spike histograms for eight simultaneously imaged AC motor neurons.

(C) Spike histograms for six simultaneously imaged GM motor neurons.

(D) Cumulative histograms of phase synchronization indices computed for pairs of identified motor neurons within the same (black) or between different (red) synergy groups. Phase synchronization was computed with (dotted) and without (solid) circular permutation of one spike histogram relative to the other.

(E and F) Phase synchronization of normalized, unpermuted spike histograms for identified neurons within the same synergy group versus proximity along the rostrocaudal (E) or dorsoventral (F) axes. Pairs of motor neurons were divided into seven equally sized groups according to proximity, data are plotted along the x axis according to the mean proximity of each group, and error bars indicate mean \pm SEM.

possibility, mice harboring a conditional *FoxP1* allele were crossed with an *Olig2::Cre* driver line to generate motor neuron selective *FoxP1^{MNA}* mutants (Dasen et al., 2008). In *FoxP1^{MNA}* mice, motor neurons fail to acquire LMC columnar and pool-specific identities and instead assume many of the features of thoracic HMC neurons. Transfated motor neurons in *FoxP1^{MNA}* mice fail to exhibit a stereotyped relationship between neuronal position and muscle target (Figure S5), yet both flexor and extensor muscles are still innervated. As a consequence, muscles co-contract, limbs are rigid, and normal locomotion is precluded (Sürmeli et al., 2011).

To assess the impact of the reversion of motor neuron identity on locomotor firing, we first monitored lumbar ventral root activities. Induction of locomotor-like activity in isolated *FoxP1^{MNA}* preparations elicited rhythmic root activity at frequencies similar to those in wild-type spinal cord (Figure S6; $p = 0.66$, Wilcoxon test). However, the normal ipsilateral alternation between L2 and L5 roots was replaced by near synchrony (Figures S7A–S7C), even though alternation between contralateral roots was still evident (data not shown). Phase differences between T9/T10 and L2 ventral root activity peaks were also similar in wild-type and *FoxP1^{MNA}* preparations (Figures S7D–S7F; $p = 0.85$, two-sample, two-tailed t test). Thus, the reversion of motor

neuron columnar fate abolishes rostrocaudal alternation in motor neuron burst firing. Nevertheless, rostral lumbar ventral root activity still provides a comparable phase reference.

To probe the cellular origins of changes in lumbar locomotor activity, we performed Ca^{2+} -sensitive fluorescence imaging of motor neurons and ventral root recording in *FoxP1^{MNA}* preparations. Motor neuron phase tuning maps (200–900 motor neurons/map; mean = 656 motor neurons) revealed substantial differences from tuning in wild-type preparations (Figures 5A–5E and Movies S3 and S4; $p = 0.0002$, Kolmogorov-Smirnov test). Motor neurons generally exhibited rhythmic firing at a common phase, close to 0° (Figure 5C), with only $\sim 2\%$ (29/1413) of *FoxP1^{MNA}* motor neurons bursting closer to 180° (Figures 5F–5J). This anomalous minority likely reflects the redundant function of *FoxP4* and thus the preservation of LMC identity in a small fraction of limb-innervating motor neurons (Dasen et al., 2008).

To exclude the possibility that motor neurons targeting certain muscles are not rhythmically active in *FoxP1^{MNA}* preparations, we analyzed the activity of identified motor neurons. *FoxP1^{MNA}* motor neurons retrogradely labeled by CTB injection into IF, AC, G, and gastrocnemius (GS, ankle extensor) muscles exhibited highly overlapping tuning distributions (IF: $-3 \pm 21^\circ$,

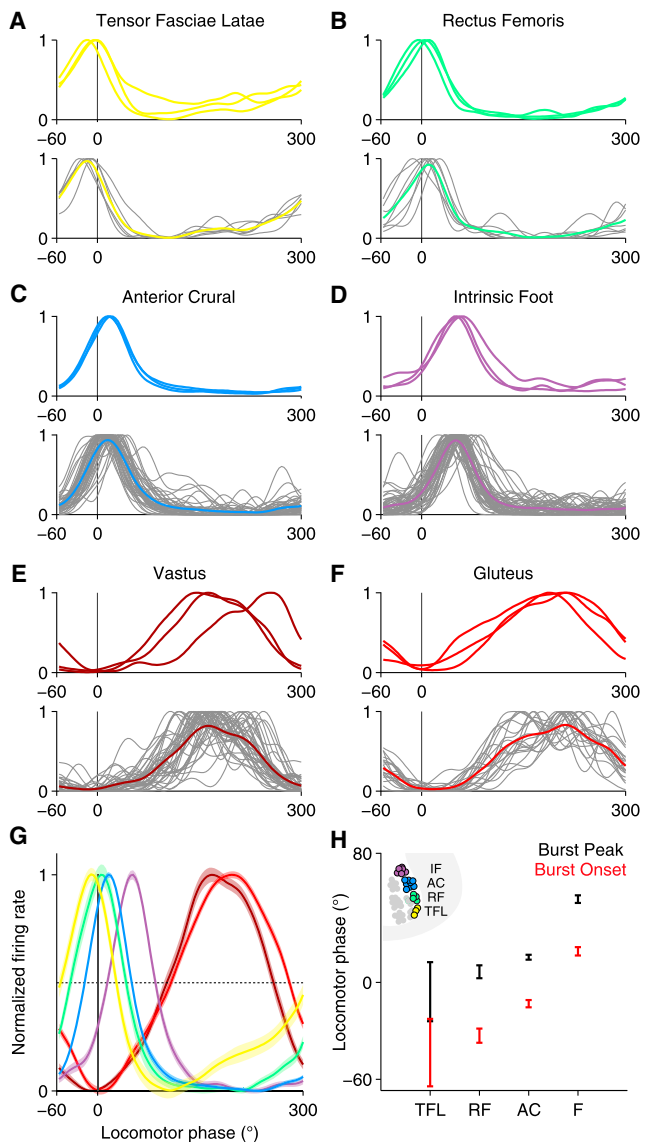


Figure 4. Cycle-Averaged Firing of Identified Motor Neurons Reveals Sequential Recruitment of Flexor Synergy Groups

(A–F) Bottom: cycle-averaged firing rates from individual CTB-labeled motor neurons (gray) imaged in a single preparation. Colored traces represent their mean. Top: mean cycle-averaged firing rates from CTB-labeled motor neurons from three different preparations for each of the six different synergy groups analyzed.

(G) Mean firing rates \pm SEM for identified motor neurons from individual synergy groups, pooled across preparations. Colors correspond to those used in (A)–(F).

(H) Median burst peak and burst onset times \pm SE of the median for four flexor synergy groups ordered by dorsoventral position (inset).

mean \pm SD, n = 46 neurons; AC: 20 \pm 26°, n = 88; G: 13 \pm 23°, n = 8; GS: -19 \pm 28°, n = 33) in marked contrast to wild-type preparations. In particular, we noted a profound conversion of extensor (G and GS) motor neuron firing to a flexor-like pattern (Figures 5D and 5E). In addition, IF motor neurons now fired slightly earlier than AC neurons, the opposite of their wild-type

relationship. We conclude that the loss of FoxP1 erodes the normal synergy group-specific patterns of motor neuron burst firing and promotes flexor monotony.

We also examined the precision with which motor neurons adopted flexor-like firing in FoxP1^{MNA} preparations. Cycle-averaged firing rates of wild-type motor neurons could be separated into two sets using k-means clustering (Figures 6A and 6B), revealing well-separated sets within individual preparations (clustering index mean \pm SEM = 3.99 \pm 0.26, n = 12 spinal cords) and across different preparations (clustering index = 3.85, n = 5,967 neurons). One set of firing rates was characterized by brief bursts (86.7 \pm 24.0° duration, mean \pm SD, n = 4,212 neurons) with phase tunings early in the locomotor cycle (13.7 \pm 27.5°). The second set exhibited prolonged bursts (165.7 \pm 46.5° duration, n = 1,755 neurons) tuned later in the locomotor cycle (166.2 \pm 46.1°). We found that 99.4% (175/176) of identified motor neurons innervating AC and IF muscles were included within the early-firing set. This finding suggests that the early- and late-firing sets are comprised of flexor and extensor motor neurons, respectively (Figures 6C and 6D).

An equivalent analysis of FoxP1^{MNA} motor neurons revealed that the cycle-averaged firing rates for virtually all neurons precisely matched those of wild-type flexor motor neurons, both in phase tuning and burst duration (Figures 6E–6H). k-means clustering failed to identify well-separated sets from individual FoxP1^{MNA} preparations (clustering index mean \pm SEM = 0.48 \pm 0.14, n = 4) or among neurons aggregated across different FoxP1^{MNA} preparations (cluster index = 0.27, n = 1,413 neurons). Cluster separation was significantly less than for wild-type firing rates ($p = 2.1 \times 10^{-6}$, one-tailed unpaired t test). Collectively, FoxP1^{MNA} motor neurons exhibited distributions of phase tuning (mean \pm SD = 12.0 \pm 42.2°) and burst duration (90.7 \pm 29.3°) that were very similar to those of the early-firing wild-type set that comprises flexor motor neurons (Figure 6F). Consistent with this, analysis of phase tuning and burst duration distributions revealed that firing exhibited 21-fold greater similarity to that of wild-type flexors than to that of extensors (Figures S7G and S7H). Taken together, our results indicate that almost all hindlimb-innervating motor neurons fire in a precisely flexor-like pattern after genetic reversion of motor neuron columnar identity.

DISCUSSION

Our analysis reveals that the identity of motor neurons determines temporal features of locomotor activation. Most critically, the reversion of LMC neurons to an ancestral HMC-like columnar character induces essentially all limb-innervating motor neurons to fire in a flexor-like pattern, a strong indication of the primacy of flexor pattern generation. We discuss below the relevance of this relationship for the current organizational state of mammalian locomotor circuits.

The Structure of Locomotor Firing at Cellular Resolution

The temporal features of motor neuron firing observed in neonatal spinal cord *in vitro* exhibit distinctions from, and commonalities with, the pattern of activation of their muscle targets in adults *in vivo*. The discrepancies imply an influence of

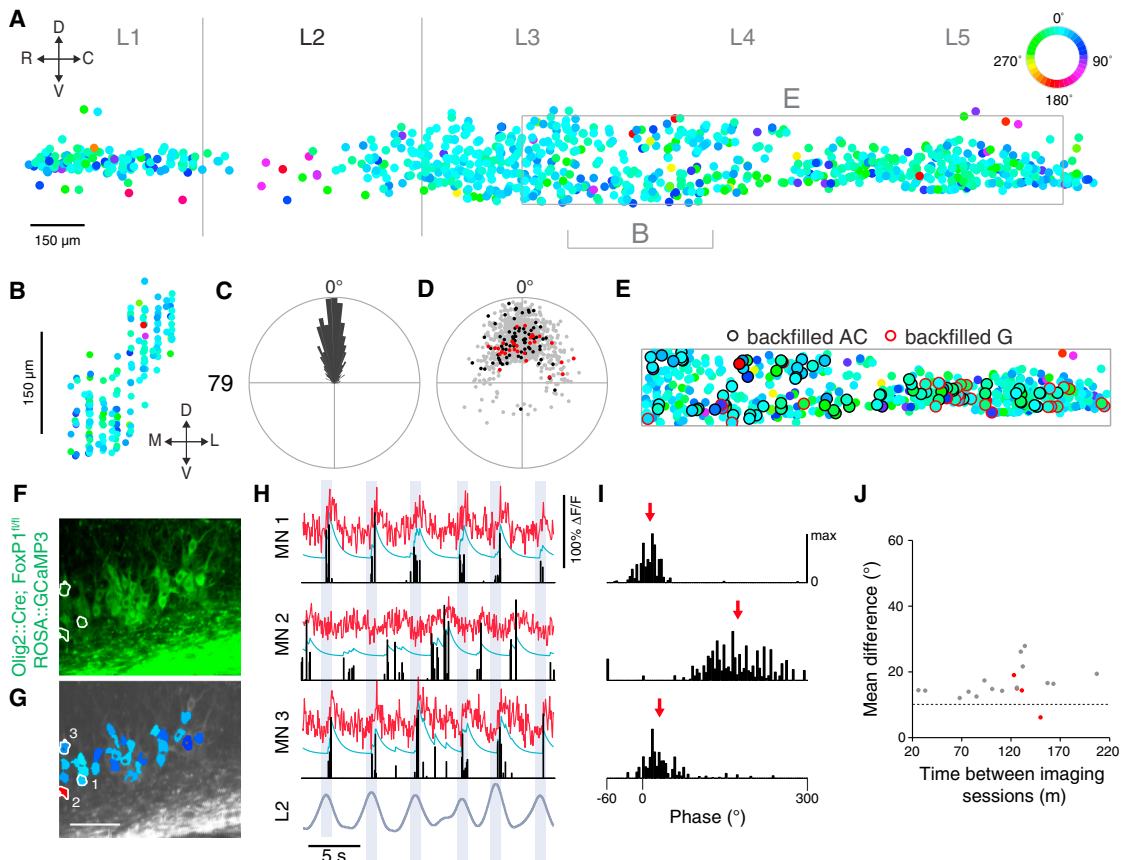


Figure 5. Uniform Motor Neuron Phase Tuning in FoxP1^{MNA} Preparations

(A) Map showing phase tuning of motor neurons within a FoxP1^{MNA} spinal cord as viewed from the lateral side (927 neurons). Segmental boundaries of the antidromically activated segment are indicated by vertical lines. Labels of other segments were drawn assuming equal segment widths.

(B) Transverse projection for the rostrocaudal extent indicated in (A).

(C) Polar histogram showing phase tuning of neurons mapped in (A). The maximal number of neurons within a single bin is shown to the left of the histogram.

(D) Polar plot indicating the phase tuning of all motor neurons mapped in (A) plotted in gray with the tunings of all CTB-labeled anterior crural (AC, black) and gluteal (G, red) motor neurons from the same preparation superimposed. The radial position of each point represents circular spread around its phase tuning.

(E) Boxed area in (A) with CTB-labeled motor neurons indicated.

(F) Single imaging field from a FoxP1^{MNA} spinal cord containing GCaMP3-expressing motor neurons (green). Scale bar is 100 μ m.

(G) ROIs for motor neurons in (F) colored according to phase tuning using the same color scale as (A).

(H) Fluorescence time courses (red) for three motor neurons from (F and G) along with spike-induced fluorescence model fit (cyan) and inferred spikes (black bars).

(I) Inferred spike counts from a full 90 s image sequence plotted across the locomotor cycle for the three motor neurons in (H), with the phase tuning of each neuron indicated (red arrows). Bin widths are 4°. Max height indicates the maximum per bin spike count.

(J) Mean tuning difference versus the interval between measurements for 4 FoxP1^{MNA} mice (red) superimposed on values from 15 wild-type mice (gray). Dotted line indicates predicted mean difference assuming stable phase tuning.

See also Figures S5 and S6 and Movies S3 and S4.

descending commands or sensory feedback in shaping locomotor pattern and potentially the refinement of circuits as the spinal cord matures.

Included among the discrepancies are differences in the number and duration of bursts. We observed that TFL and RF motor neurons burst only once per locomotor cycle *in vitro*, yet their target muscles exhibit dual burst activity in many locomotor contexts *in vivo* (Rossignol, 1996; Yakovenko et al., 2002). This difference likely reflects sensory feedback, inducing a second phase of motor neuron bursting per cycle, or shifting the firing phase of a subset of neurons within the TFL and RF pools (Loeb, 1985; Perret and Cabelguen, 1980). A second distinction

is that flexor motor neurons exhibit relatively brief bursts *in vitro*, whereas flexor muscle activation *in vivo* can occupy a much greater proportion of the locomotor cycle. Studies in cats and mice *in vivo* suggest that the duration of muscle activation is also governed by sensory feedback, in part through the regulation of muscle offset timing (Akay et al., 2014; Lam and Pearson, 2001). Together, these findings suggest that spinal circuits are sufficient to produce a basic dynamical template of locomotor activity that is subject to refinement through sensory feedback.

Nevertheless, conserved features emerge from a comparison of locomotor patterns *in vitro* and *in vivo*, most clearly in the timing of recruitment of mouse motor neurons that innervate

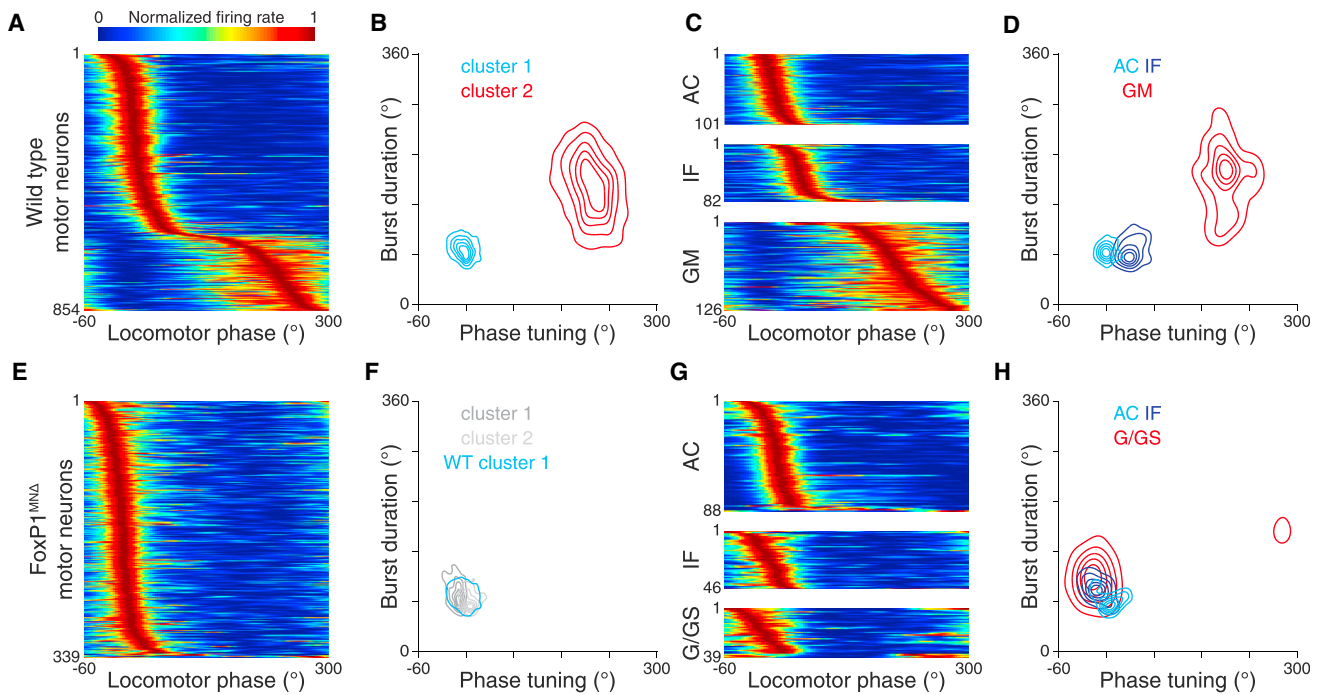


Figure 6. Prevalence of Flexor-like Firing in FoxP1^{MNA} Motor Neurons

- (A) Cycle-averaged firing rates for 854 motor neurons obtained from one wild-type preparation.
- (B) Kernel density plots of the joint distribution of phase tuning and burst duration for 5,967 motor neurons pooled across 14 preparations and clustered into two sets.
- (C) Cycle-averaged firing rates for identified anterior crural (AC), intrinsic foot (IF), and gluteal extensor (GM) motor neurons, pooled across all wild-type preparations.
- (D) Kernel density plots of the joint distribution of phase tuning and burst duration for identified wild-type motor neurons.
- (E) Cycle-averaged firing rates for 339 motor neurons from one FoxP1^{MNA} preparation.
- (F) Kernel density plots of the joint distribution of phase tuning and burst duration for 1,413 imaged FoxP1^{MNA} motor neurons pooled across 4 mice and clustered into two sets. Overlaid in cyan is the 1/6th of maximum contour from the early firing set derived from wild-type data shown in (B).
- (G) Cycle-averaged firing rates for identified anterior crural (AC), intrinsic foot (IF), gluteal (G), or gastrocnemius (GS) motor neurons in FoxP1^{MNA} mice, pooled across four FoxP1^{MNA} preparations.
- (H) Kernel density plots of the joint distribution of phase tuning and burst duration for FoxP1^{MNA} motor neurons retrogradely labeled from AC, IF, G, and GS muscles.

See also Figure S7.

synergist muscles acting on different joints. Our findings indicate that local circuits are sufficient to direct the activation of motor neurons innervating synergistic flexor muscles in a ventral-to-dorsal sequence that matches the proximodistal order of their muscle targets. EMG recordings from mouse hindlimb muscles during walking document the onset of hip, knee, and ankle flexor muscle activation in a similar proximodistal order (Akay et al., 2014). In cat, however, muscle activation sequences do not necessarily conform to the recruitment order we observe *in vitro* in mouse (Krouchev et al., 2006; Rossignol, 1996; Yako-venko et al., 2002). Such differences could reflect developmental changes, interspecies differences in local circuit wiring, or the added influence of descending commands and sensory feedback. The activation sequence we observed *in vitro* implies that premotor interneurons are able to recognize and select from synergy groups governing different limb joints.

We emphasize that two-photon Ca²⁺ imaging reveals aspects of the organization of locomotor firing across the LMC that could

not have been discerned from motor nerve or muscle recordings, which conflate the activity of individual motor neurons. The high spatial resolution afforded by imaging revealed that motor neurons exhibit abrupt changes in firing at the boundaries between synergy groups. The spatial resolution and broad coverage provided by our datasets were critical in exposing spatially extended synchrony. Cellular resolution estimates of neuronal firing were also necessary to delineate the precision of flexor firing and its predominance among FoxP1^{MNA} motor neurons.

Our observations also point to the inadequacy of monitoring ventral root activity alone when probing the organization of mammalian locomotor circuits. Interpretations of *in vitro* ventral root recordings have typically relied upon the notion that L2 and L5 root activity peaks reflect, respectively, flexor and extensor motor neuron firing phases. Our findings document sizeable populations of motor neurons that exhibit distinct flexor or extensor firing patterns at each lumbar segment. Differences in

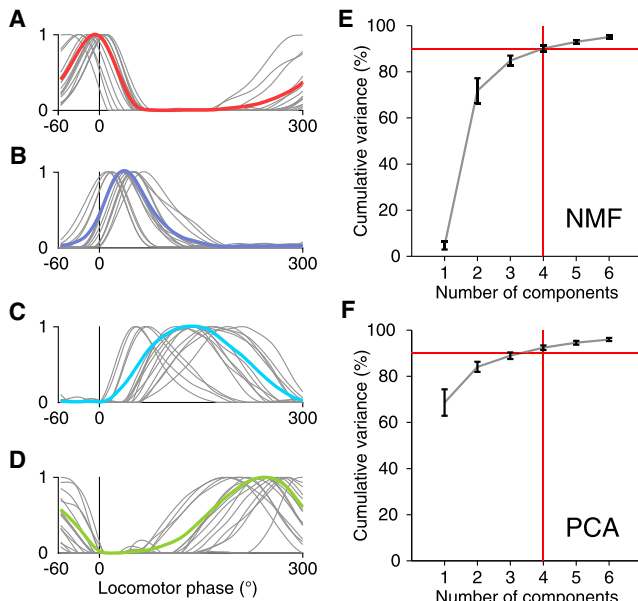


Figure 7. Basic Patterns Extracted from In Vitro Neonatal Mouse Locomotor Firing

(A–D) Components resulting from applying non-negative matrix factorization (NMF) to the cycle-averaged firing rates obtained from 15 wild-type spinal cords (with number of components set to four). Gray lines represent components from individual spinal cords, and colored lines represent means across all spinal cords.

(E) Cumulative variance explained by adding additional components. Red lines indicate the number of components necessary to account for ~90% of the cumulative variance. Error bars represent mean values \pm SD.

(F) Format matches (E), except each dataset was decomposed using principal component analysis (PCA) instead of NMF.

the number of flexor and extensor motor neurons across segments and/or differences in motor neuron firing rate (Yakovenko et al., 2002) could contribute to this discrepancy. Clearly, a reliance on ventral root activity peaks ignores the extent of diversity in motor neuron activities present at individual segmental levels of the spinal cord.

At first glance, the heterogeneous firing patterns across different flexor synergy groups appear inconsistent with a recent analysis of ventral root recordings from isolated neonatal rat spinal cord (Dominici et al., 2011). This study concluded that locomotor output from neonatal preparations is well approximated by two alternating rhythmic patterns, in contrast to the greater complexity seen in EMG recordings from behaving adults. This discrepancy prompted us to perform an analysis similar to that of Dominici et al. (2011) but using the cycle-averaged firing rates of the many motor neurons we recorded in individual neonatal spinal cords. Non-negative matrix factorization revealed that four components are needed to explain ~90% of the variance in locomotor firing across the neonatal LMC, as in adult EMG (Figures 7A–7E). Similar results were obtained using principal-component analysis (Figure 7F). Thus, the complexity of locomotor output from the isolated neonatal rodent spinal cord is similar to that generated in adults *in vivo*, contrary to the conclusion of Dominici et al. (2011).

Locomotor Pattern and the Recognition of Flexor and Extensor Motor Neurons

What explains the finding that essentially all limb-innervating motor neurons fire in a flexor-like pattern after FoxP1^{MNA}-mediated reversion of motor neuron identity?

One possibility is that LMC neurons play an active role in the differentiation or function of pattern-generating circuits. The reversion of motor neuron identity may undermine the formation of extensor circuits, leaving, by default, a monophasic flexor system. Mechanistically, LMC neurons could be the source of a secreted signal that instructs the assembly of extensor circuits. In fact, there is precedent for the secretion by LMC motor neurons of a signal, retinoic acid, which drives the diversification of limb-innervating motor neurons (Sockanathan and Jessell, 1998). Alternatively, synaptic feedback from LMC motor neurons may be necessary for extensor pattern generation. Recruitment of Renshaw inhibitory or equivalent excitatory interneurons by motor neuron axon collaterals might influence ongoing interneuron network activity (Alvarez and Fyffe, 2007; Machacek and Hochman, 2006; O'Donovan et al., 2010).

A second scenario is suggested by the apparent ability of premotor interneurons to discriminate flexor and extensor motor neurons. The ancestral similarity of flexor LMC and HMC motor neurons may lead to the expression of shared surface recognition features on these two motor neuron classes, permitting flexor but not extensor premotor interneurons to form connections with ancestrally reverted motor neurons. In this view, normal premotor activity would be preserved in FoxP1^{MNA} spinal cord, but extensor premotor interneurons would fail to recognize HMC-like motor neurons. The finding that a small minority of motor neurons with extensor-like firing are still present in FoxP1^{MNA} preparations indicates that extensor premotor circuits are at least in part preserved. In addition, the scattered distribution of the few extensor-firing motor neurons in FoxP1^{MNA} preparations implies that premotor interneurons are able to select individual target motor neurons with precision.

The Evolutionary Primacy of Flexor Pattern Generation

Whether extensor pattern generation is diminished or HMC-like motor neurons recruit only flexor interneuronal input, the prevalence of flexor firing in FoxP1^{MNA} preparations provides strong support for the evolutionary primacy of flexor pattern generation. In mammals, the phasic continuity evident between limb flexor and thoracic ventral root activity and the similarity between wave-like patterns in mammalian thoracic and primitive vertebrate motor output are consistent with the idea that flexor pattern generation emerged by co-opting primitive swim circuits. This implies that paired flexor and extensor patterns did not emerge jointly at the evolutionary onset of limb-based locomotion. In the direct ancestors of tetrapods, the extensor system may have evolved as a later elaboration of spinal circuitry to promote ground repulsion through limb extension.

That the basic organization of modern flexor circuits predates the evolutionary emergence of extensor circuits further implies that the generation of flexor-like pattern can occur without opponent input from extensor premotor circuits. This view agrees with the subordinate nature of extensor pattern generation suggested by certain observations. Notably, locomotor firing in mice and

cats is subject to brief and sporadic periods of quiescence, termed “deletions,” that persist for several cycles. Flexor burst deletions are accompanied by tonic extensor motor neuron firing, whereas flexor motor neuron bursting continues unabated during extensor burst deletions (Duyens, 1977, 2006; Zhong et al., 2012). Other studies have indicated that the rhythm of locomotor firing may be determined by populations of interneurons that burst exclusively in flexor phase and, in turn, drive pattern-forming circuits (Brownstone and Wilson, 2008; Pearson and Duyens, 1976), which could at least partly explain how flexor dominance is imposed. Taken together with our findings, these results suggest that the late addition of extensor pattern, coupled with the need for flexor-extensor coordination, led to an asymmetric dependence in pattern-generating circuits, with flexor circuits having a dominant role.

Genetic studies have shown that locomotor firing persists after the loss of any single cardinal interneuron population (Crone et al., 2008; Gosgnach et al., 2006; Lanuza et al., 2004; Zhang et al., 2008), suggesting that the generation of locomotor firing can be achieved through a diverse array of interneuron network architectures. In addition, modeling studies have shown that locomotor-like activity patterns can be read out from neural networks permitted considerable flexibility in their connectivity, as long as the network outputs are weighted appropriately (Sussillo and Abbott, 2009). In this context, and with a new emphasis on motor neuron recognition, it is conceivable that interneuronal connectivity in locomotor circuits is only weakly constrained, whereas output connections onto motor pools are precisely specified.

EXPERIMENTAL PROCEDURES

All experiments and procedures were performed according to NIH guidelines and approved by the Institutional Animal Care and Use Committee of Columbia University.

Retrograde Labeling of Motor Neurons

Motor neurons were retrogradely labeled *in vivo* at P1–P3 via intramuscular injections of cholera toxin B subunit conjugated to Alexa 555 or 647 (CTB; Life Technologies) (Sürmeli et al., 2011).

Spinal Cord Preparation

Spinal cords were removed from mice, aged 2–5 days postnatal, and submerged in artificial cerebrospinal fluid (ACSF) held at constant temperature (24–25°C). Suction electrode recordings were simultaneously obtained from multiple ventral roots. Ca²⁺ transients were measured from GCaMP3-expressing LMC motor neurons in a single segment while the corresponding ventral root was antidromically stimulated to evoke motor neuron activity, enabling the calibration of the model of spike-related fluorescence fluctuations we used for spike inference. Subsequently, locomotor firing was induced by adding a cocktail of rhythmic agonists to the ACSF (5 μM NMDA, 10 μM 5-HT, 50 μM DA). Starting 1 hr later, we collected fluorescence image sequences throughout the imageable extent of the LMC.

Two-Photon Microscopy

An Ultima microscope (Prairie Technologies) with a 20× objective (1.0 numerical aperture, 2 mm working distance; XLUMPLFLN, Olympus) was used to acquire all fluorescence images (256 × 256 pixels/frame). GCaMP3 was excited using a Chameleon Ultra II laser (Coherent) tuned to 940 nm and, in 17 of 19 preparations, raster scanned across the preparation at 60 Hz using a resonant galvanometer. These signals were downsampled to 15 Hz to increase the

signal-to-noise ratio. In 2 of 19 preparations, the laser was scanned at 8 Hz with conventional 6 mm galvanometers in a spiral trajectory. GCaMP3 emission was collected using a GaAsP photomultiplier tube (Hamamatsu; 525/50 emission filter).

Data Analysis

The centroids of motor neuron somata were manually defined in ImageJ and used to demarcate a preliminary region of interest (ROI) around each soma. These ROIs were further refined using automated MATLAB scripts to include only those pixels likely to arise from each soma. Time series of ROI-averaged fluorescence fluctuations ($\Delta F/F$) were processed using a spike inference algorithm. Phase-tuning values were computed relative to peaks in simultaneously obtained ventral root recordings using inferred spiking activity.

SUPPLEMENTAL INFORMATION

Supplemental Information includes Supplemental Experimental Procedures, seven figures, and four movies and can be found with this article online at <http://dx.doi.org/10.1016/j.cell.2015.06.036>.

AUTHOR CONTRIBUTIONS

T.A.M. and T.M.J. devised the project. T.A.M., T.M.J., and A.M. designed experiments. T.A.M. constructed experimental apparatus, performed the experiments, and wrote core data processing scripts. T.A.M. and A.M. analyzed data. T.A.M., E.P., L.P., and A.M. developed data analytical techniques. E.P and L.P. contributed unpublished spike inference algorithms. T.A.M., T.M.J., and A.M. interpreted data and wrote the manuscript.

ACKNOWLEDGMENTS

We are grateful to D. Wu for assistance with mouse genotyping; M. Mendelsohn and N. Zabello for animal care; H. Tucker for the conditional *FoxP1* strain; Y. Ivanenko for advice about analysis; and B. Han, K. MacArthur, S. Morton, and I. Schieren for technical assistance. We thank G.Z. Mantis for the custom-built recording stage used in the electrophysiology experiments and for advice about experimental approaches. We are grateful to R. Axel, E. Azim, J. Bikoff, R. Brownstone, S. Druckmann, A. Fink, A. Karpova, A. Murray, and J. de Nooij for helpful comments on the work and manuscript. T.A.M. was supported by the NSF Graduate Research Fellowship Program. L.P. was supported by DARPA W91NF-14-1-0269, ARO MURI W911NF-12-1-0594, NSF CAREER award IOS-0641912, and Simons Foundation Global Brain Research Award 325398. T.M.J. was supported by NIH grant NS033245, the Harold and Leila Y. Mathers Foundation, and Project A.L.S. and is an investigator of the Howard Hughes Medical Institute. A.M. is a Howard Hughes Medical Institute Fellow of the Helen Hay Whitney Foundation.

Received: January 19, 2015

Revised: April 1, 2015

Accepted: May 21, 2015

Published: July 16, 2015

REFERENCES

- Akay, T., Tourtellotte, W.G., Arber, S., and Jessell, T.M. (2014). Degradation of mouse locomotor pattern in the absence of proprioceptive sensory feedback. *Proc. Natl. Acad. Sci. USA* **111**, 16877–16882.
- Alvarez, F.J., and Fyffe, R.E. (2007). The continuing case for the Renshaw cell. *J. Physiol.* **584**, 31–45.
- Beliez, L., Barrière, G., Bertrand, S.S., and Cazalets, J.R. (2015). Origin of thoracic spinal network activity during locomotor-like activity in the neonatal rat. *J. Neurosci.* **35**, 6117–6130.
- Berens, P. (2009). CircStat: a MATLAB toolbox for circular statistics. *J. Stat. Softw.* **31**, 1–21.

- Bonnot, A., Whelan, P.J., Mentis, G.Z., and O'Donovan, M.J. (2002). Spatio-temporal pattern of motoneuron activation in the rostral lumbar and the sacral segments during locomotor-like activity in the neonatal mouse spinal cord. *J. Neurosci.* 22, RC203.
- Bonnot, A., Mentis, G.Z., Skoch, J., and O'Donovan, M.J. (2005). Electroporation loading of calcium-sensitive dyes into the CNS. *J. Neurophysiol.* 93, 1793–1808.
- Brown, T.G. (1914). On the nature of the fundamental activity of the nervous centres; together with an analysis of the conditioning of rhythmic activity in progression, and a theory of the evolution of function in the nervous system. *J. Physiol.* 48, 18–46.
- Brownstone, R.M., and Wilson, J.M. (2008). Strategies for delineating spinal locomotor rhythm-generating networks and the possible role of Hb9 interneurons in rhythmodogenesis. *Brain Res. Brain Res. Rev.* 57, 64–76.
- Burke, R.E., Degtyarenko, A.M., and Simon, E.S. (2001). Patterns of locomotor drive to motoneurons and last-order interneurons: clues to the structure of the CPG. *J. Neurophysiol.* 86, 447–462.
- Crone, S.A., Quinlan, K.A., Zagoraiou, L., Droho, S., Restrepo, C.E., Lundfalld, L., Endo, T., Setlak, J., Jessell, T.M., Kiehn, O., and Sharma, K. (2008). Genetic ablation of V2a ipsilateral interneurons disrupts left-right locomotor coordination in mammalian spinal cord. *Neuron* 60, 70–83.
- Dasen, J.S., De Camilli, A., Wang, B., Tucker, P.W., and Jessell, T.M. (2008). Hox repertoires for motor neuron diversity and connectivity gated by a single accessory factor, FoxP1. *Cell* 134, 304–316.
- De Marco Garcia, N.V., and Jessell, T.M. (2008). Early motor neuron pool identity and muscle nerve trajectory defined by postmitotic restrictions in Nkx6.1 activity. *Neuron* 57, 217–231.
- Dominici, N., Ivanenko, Y.P., Cappellini, G., d'Avella, A., Mondi, V., Cicchese, M., Fabiano, A., Silei, T., Di Paolo, A., Giannini, C., et al. (2011). Locomotor primitives in newborn babies and their development. *Science* 334, 997–999.
- Duyens, J. (1977). Reflex control of locomotion as revealed by stimulation of cutaneous afferents in spontaneously walking premammillary cats. *J. Neurophysiol.* 40, 737–751.
- Duyens, J. (2006). How deletions in a model could help explain deletions in the laboratory. *J. Neurophysiol.* 95, 562–563, author reply 563–565.
- Falgairette, M., and Cazalets, J.-R. (2007). Metachronal coupling between spinal neuronal networks during locomotor activity in newborn rat. *J. Physiol.* 580, 87–102.
- Gosgnach, S., Lanuza, G.M., Butt, S.J., Saueressig, H., Zhang, Y., Velasquez, T., Riethmacher, D., Callaway, E.M., Kiehn, O., and Goulding, M. (2006). V1 spinal neurons regulate the speed of vertebrate locomotor outputs. *Nature* 440, 215–219.
- Grillner, S., and Wallén, P. (2002). Cellular bases of a vertebrate locomotor system-steering, intersegmental and segmental co-ordination and sensory control. *Brain Res. Brain Res. Rev.* 40, 92–106.
- Grillner, S., and Zanger, P. (1975). How detailed is the central pattern generation for locomotion? *Brain Res.* 88, 367–371.
- Helmchen, F., and Tank, D.W. (2005). A single-compartment model of calcium dynamics in nerve terminals and dendrites. In *Imaging in Neuroscience and Development*, R. Yuste and A. Konnerth, eds. (Cold Spring Harbor Laboratory Press), pp. 265–275.
- Kiehn, O., and Kjaerulff, O. (1996). Spatiotemporal characteristics of 5-HT and dopamine-induced rhythmic hindlimb activity in the in vitro neonatal rat. *J. Neurophysiol.* 75, 1472–1482.
- Krouchev, N., Kalaska, J.F., and Drew, T. (2006). Sequential activation of muscle synergies during locomotion in the intact cat as revealed by cluster analysis and direct decomposition. *J. Neurophysiol.* 96, 1991–2010.
- Kudo, N., and Yamada, T. (1987). N-methyl-D,L-aspartate-induced locomotor activity in a spinal cord-hindlimb muscles preparation of the newborn rat studied in vitro. *Neurosci. Lett.* 75, 43–48.
- Kusakabe, R., and Kuratani, S. (2005). Evolution and developmental patterning of the vertebrate skeletal muscles: perspectives from the lamprey. *Dev. Dyn.* 234, 824–834.
- Kwan, A.C., Dietz, S.B., Webb, W.W., and Harris-Warrick, R.M. (2009). Activity of Hb9 interneurons during fictive locomotion in mouse spinal cord. *J. Neurosci.* 29, 11601–11613.
- Lam, T., and Pearson, K.G. (2001). Proprioceptive modulation of hip flexor activity during the swing phase of locomotion in decerebrate cats. *J. Neurophysiol.* 86, 1321–1332.
- Lanuza, G.M., Gosgnach, S., Pierani, A., Jessell, T.M., and Goulding, M. (2004). Genetic identification of spinal interneurons that coordinate left-right locomotor activity necessary for walking movements. *Neuron* 42, 375–386.
- Loeb, G.E. (1985). Motoneurone task groups: coping with kinematic heterogeneity. *J. Exp. Biol.* 115, 137–146.
- Lowell, B., Olson, D., and Yu, J. (2006). Development and phenotype of ChAT-IRES-Cre mice. MGI Direct Data Submission. <http://www.informatics.jax.org/reference/J:114556>.
- Machacek, D.W., and Hochman, S. (2006). Noradrenaline unmasks novel self-reinforcing motor circuits within the mammalian spinal cord. *J. Neurosci.* 26, 5920–5928.
- McCrea, D.A., and Rybak, I.A. (2008). Organization of mammalian locomotor rhythm and pattern generation. *Brain Res. Brain Res. Rev.* 57, 134–146.
- McHanwell, S., and Bischof, T.J. (1981). The localization of motoneurons supplying the hindlimb muscles of the mouse. *Philos. Trans. R. Soc. Lond. B Biol. Sci.* 293, 477–508.
- Mormann, F., Lehnertz, K., David, P., and Elger, C.E. (2000). Mean phase coherence as a measure for phase synchronization and its application to the EEG of epilepsy patients. *Physica D* 144, 358–369.
- O'Donovan, M.J., Bonnot, A., Mentis, G.Z., Arai, Y., Chub, N., Schneider, N.A., and Wenner, P. (2008). Imaging the spatiotemporal organization of neural activity in the developing spinal cord. *Dev. Neurobiol.* 68, 788–803.
- O'Donovan, M.J., Bonnot, A., Mentis, G.Z., Chub, N., Pujala, A., and Alvarez, F.J. (2010). Mechanisms of excitation of spinal networks by stimulation of the ventral roots. *Ann. N Y Acad. Sci.* 1198, 63–71.
- Pearson, K., and Duyens, J. (1976). Function of segmental reflexes in the control of stepping in cockroaches and cats. In *Neural Control of Locomotion*, Vol. 18, Herman R., Grillner S., Stein P., and Stuart D., eds. (Plenum Press), pp. 519–537.
- Perret, C., and Cabelguen, J.-M. (1980). Main characteristics of the hindlimb locomotor cycle in the decorticate cat with special reference to bifunctional muscles. *Brain Res.* 187, 333–352.
- Platzer, W. (2004). *Color Atlas of Human Anatomy, Volume 1: Locomotor System* (Thieme).
- Pnevmatikakis, E.A., Gao, Y., Soudry, D., Pfau, D., Lacefield, C., Poskanzer, K., Bruno, R., Yuste, R., and Paninski, L. (2014). A structured matrix factorization framework for large scale calcium imaging data analysis. arXiv, arXiv:14092903, <http://arxiv.org/abs/1409.2903>.
- Rossignol, S. (1996). Neural control of stereotypic limb movements. In *Handbook of Physiology, Exercise: Regulation and Integration of Multiple Systems*, L. Rowell and J. Shepherd, eds. (Oxford University Press), pp. 173–216.
- Rousso, D.L., Gaber, Z.B., Wellik, D., Morrisey, E.E., and Novitch, B.G. (2008). Coordinated actions of the forkhead protein Foxp1 and Hox proteins in the columnar organization of spinal motor neurons. *Neuron* 59, 226–240.
- Sockanathan, S., and Jessell, T.M. (1998). Motor neuron-derived retinoid signaling specifies the subtype identity of spinal motor neurons. *Cell* 94, 503–514.
- Sürmeli, G., Akay, T., Ippolito, G.C., Tucker, P.W., and Jessell, T.M. (2011). Patterns of spinal sensory-motor connectivity prescribed by a dorsoventral positional template. *Cell* 147, 653–665.

- Sussillo, D., and Abbott, L.F. (2009). Generating coherent patterns of activity from chaotic neural networks. *Neuron* 63, 544–557.
- Talpalar, A.E., Endo, T., Löw, P., Borgius, L., Hägglund, M., Dougherty, K.J., Ryge, J., Hnasko, T.S., and Kiehn, O. (2011). Identification of minimal neuronal networks involved in flexor-extensor alternation in the mammalian spinal cord. *Neuron* 71, 1071–1084.
- Vanderhorst, V.G., and Holstege, G. (1997). Organization of lumbosacral motoneuronal cell groups innervating hindlimb, pelvic floor, and axial muscles in the cat. *J. Comp. Neurol.* 382, 46–76.
- Yakovenko, S., Mushahwar, V., VanderHorst, V., Holstege, G., and Prochazka, A. (2002). Spatiotemporal activation of lumbosacral motoneurons in the locomotor step cycle. *J. Neurophysiol.* 87, 1542–1553.
- Zariwala, H.A., Borghuis, B.G., Hoogland, T.M., Madisen, L., Tian, L., De Zeeuw, C.I., Zeng, H., Looger, L.L., Svoboda, K., and Chen, T.W. (2012). A Cre-dependent GCaMP3 reporter mouse for neuronal imaging in vivo. *J. Neurosci.* 32, 3131–3141.
- Zhang, Y., Narayan, S., Geiman, E., Lanuza, G.M., Velasquez, T., Shanks, B., Akay, T., Dyck, J., Pearson, K., Gosgnach, S., et al. (2008). V3 spinal neurons establish a robust and balanced locomotor rhythm during walking. *Neuron* 60, 84–96.
- Zhang, J., Lanuza, G.M., Britz, O., Wang, Z., Siembab, V.C., Zhang, Y., Velasquez, T., Alvarez, F.J., Frank, E., and Goulding, M. (2014). V1 and v2b interneurons secure the alternating flexor-extensor motor activity mice require for limbed locomotion. *Neuron* 82, 138–150.
- Zhong, G., Shevtsova, N.A., Rybak, I.A., and Harris-Warrick, R.M. (2012). Neuronal activity in the isolated mouse spinal cord during spontaneous deletions in fictive locomotion: insights into locomotor central pattern generator organization. *J. Physiol.* 590, 4735–4759.

Supplemental Figures

Cell

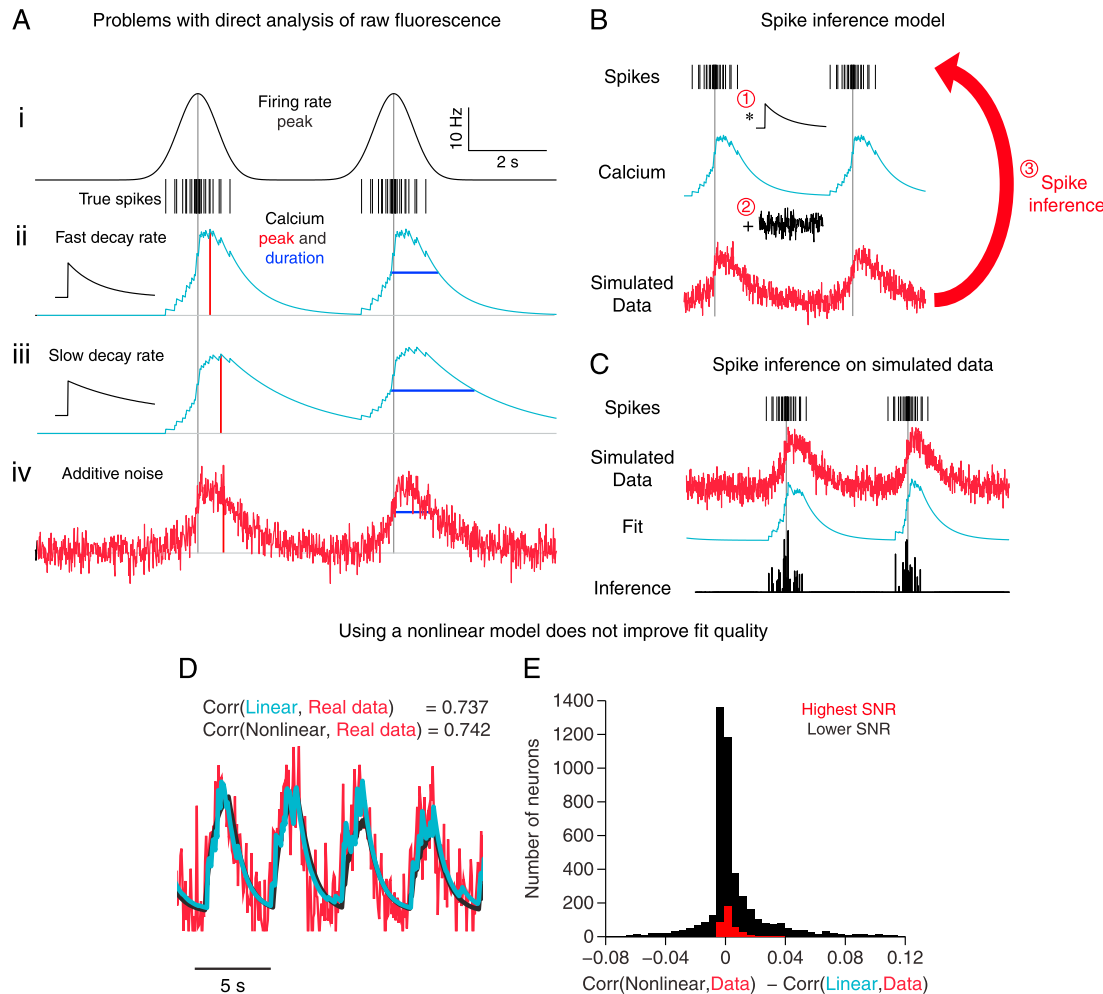


Figure S1. Spike Inference Is a Justifiable Approach for Analyzing Ca^{2+} Imaging Data, Related to Figure 1

(A) Schematic depicting the relationship between firing and Ca^{2+} . (i) Model firing rate with bursts peaking at 20 Hz (top) and underlying Poisson spike train (bottom). The spike train is identical during both bursts. Extended vertical black lines indicate the time of peak firing rate during each burst. (ii) Convolving a fast-decaying Ca^{2+} kernel (black; left) with the spike train shown in (i) results in a Ca^{2+} time series (cyan; right). Red bars denote the time of the Ca^{2+} peak. Blue lines indicate burst duration as measured from the Ca^{2+} signal (defined as full width at half maximum amplitude). (iii) The convolution of the spike train from (i) with a slower-decaying kernel (black; left) results in the time series shown (cyan; right). Variability in the Ca^{2+} indicator decay rate makes the comparison of burst duration measurements taken from different preparations difficult. (iv) Gaussian noise was added to the Ca^{2+} time series from (ii) in order to simulate noisy fluorescence measurements, in which both the Ca^{2+} peak and duration are obscured.

(B) Our spike inference algorithm used a simple model that assumed fluorescence measurements arose from a spike train convolved with a single-exponential kernel (1; assumption validated in panels D-E of this figure), with additive Gaussian noise (2; assumption validated in Figures S2D and S2E). The algorithm inverted this model (3; assumption validated in Figures S2F-S2H) to find the most likely spike histogram underlying each fluorescence time series.

(C) Example showing performance of spike inference on simulated data (red) plotted above the spike inference model fit (cyan) and inferred spikes (black bars).

(D) A fluorescence time series measured from a motor neuron (red), together with the predicted Ca^{2+} signal derived from either a linear model of Ca^{2+} dynamics (cyan) or a nonlinear model (black).

(E) Histogram comparing the differences between linear and nonlinear model fit quality, as measured using the Pearson correlation (Corr) between measured fluorescence and model prediction. This difference, $\text{Corr}(\text{linear prediction, data}) - \text{Corr}(\text{nonlinear prediction, data})$, is shown for 4,944 neurons that were each imaged as they were antidromically driven to fire in defined patterns (as shown in Figures S2D and S2E). Red bars show a subset of high SNR neurons ($n = 367$) that were used to estimate the fluorescence transient decay rate.

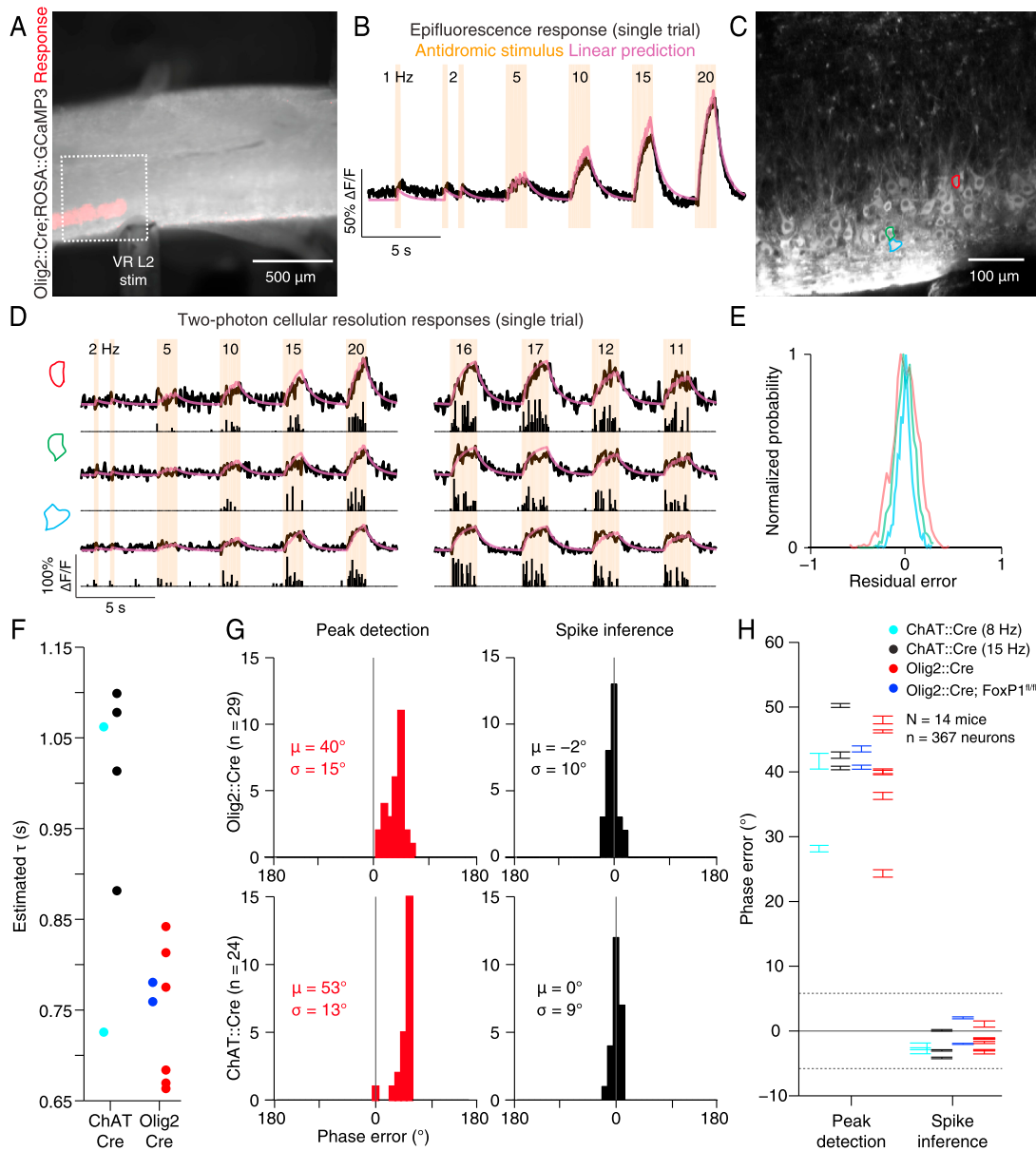


Figure S2. Validation of Spike Inference Using Antidromic Motor Neuron Activation, Related to Figure 1

(A) Sagittal view of L2 during antidiromic stimulation taken under epifluorescence illumination. The region responsive to antidiromic stimulation is shown in red.

(B) Average response to the antidiromic stimulus (orange; numbers show stimulation rate during each stimulus train in Hz) across the red region shown in (A). The convolution of the antidiromic stimulus and an exponentially decaying kernel is superimposed upon the average fluorescence time series (purple), and represents the predicted Ca^{2+} response to the antidiromic stimulus under our Ca^{2+} model.

(C) Two-photon imaging field (dotted region in (A)) containing example motor neurons that were responsive to antidiromic stimulation (colored ROIs).

(D) Fluorescence time series (black) from three ROIs in (C) during antidiromic stimulation (orange; numbers show stimulation rate during each stimulus in Hz). The predicted Ca^{2+} response is shown in purple and the inferred spikes underlying each fluorescence time series are shown as black bars.

(E) Histograms of the residual error between the fluorescence time series and predicted Ca^{2+} response for each of the three responses shown in (D).

(F) Estimated decay time constants in seconds for each dataset plotted in (H). Colors correspond to different experimental conditions (legend in (H)).

(G) Comparison of peak detection and spike inference approaches to phase tuning estimation. Phase tuning was estimated using a simple peak detection method (left), or using spike inference (right). Phase tuning was estimated using fluorescence data taken from four antidiromic bursts (shown in the left panel of (D)). The midpoint of each burst was defined as 0° . Histograms showing phase tuning estimation error from $n = 29$ motor neurons from a single *ChAT::Cre* mouse (top) and $n = 24$ motor neurons from a single *Olig2::Cre* mouse (bottom).

(H) Error distributions for each mouse preparation calibrated during antidiromic stimulation using peak detection (left) or spike inference (right) to estimate phase. Error bars span the mean \pm SEM. This analysis reveals that spike inference successfully reduces phase error that arises due to the temporal delay between peak calcium and peak firing rate, and due to variation in calcium decay rates between preparations.

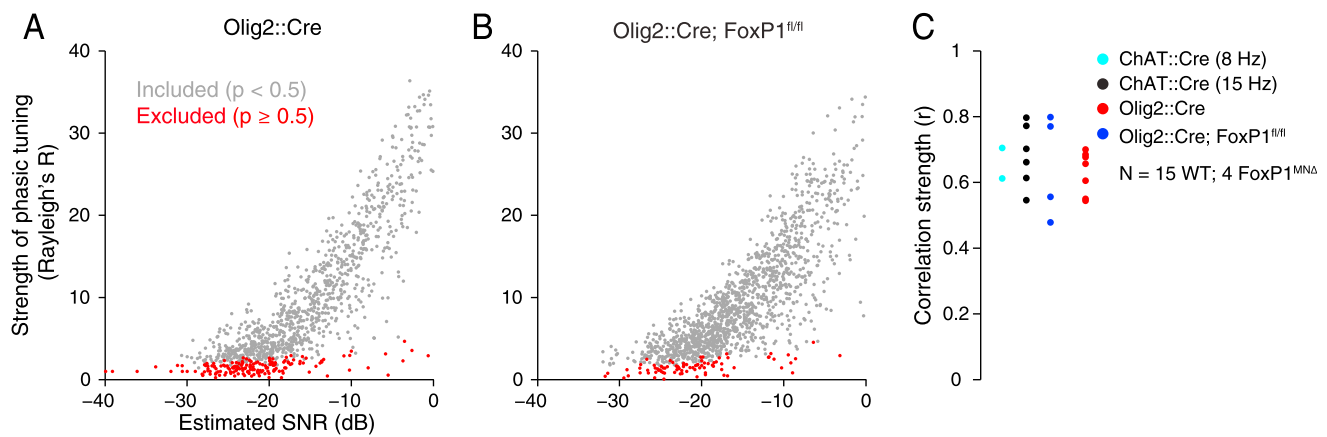


Figure S3. Correlation between Signal Quality and Phase Tuning Strength, Related to Figure 2

(A) Correlation between estimated signal-to-noise ratio (SNR) and the R statistic from Rayleigh's test of circular uniformity for all imaged motor neurons in a single *Olig2::Cre* mouse. Red points denote imaged motor neurons that were excluded from further analysis because they had Rayleigh's test P values > 0.5 .

(B) Same format as (A) in a *FoxP1^{MNA}* preparation.

(C) The correlation between R and SNR was high in all wild-type preparations (Pearson correlation = 0.54-0.80, mean = 0.66, n = 15 wild-type spinal cords) indicating that much of the pattern of motor neuron firing is captured by its phase tuning. This correlation seen in wild-type data was statistically indistinguishable from the correlation measured in *FoxP1^{MNA}* data (Pearson correlation = 0.48-0.80, mean = 0.65, n = 4 spinal cords; comparison to wild-type: p = 0.94, two-sample, two-tailed t test).

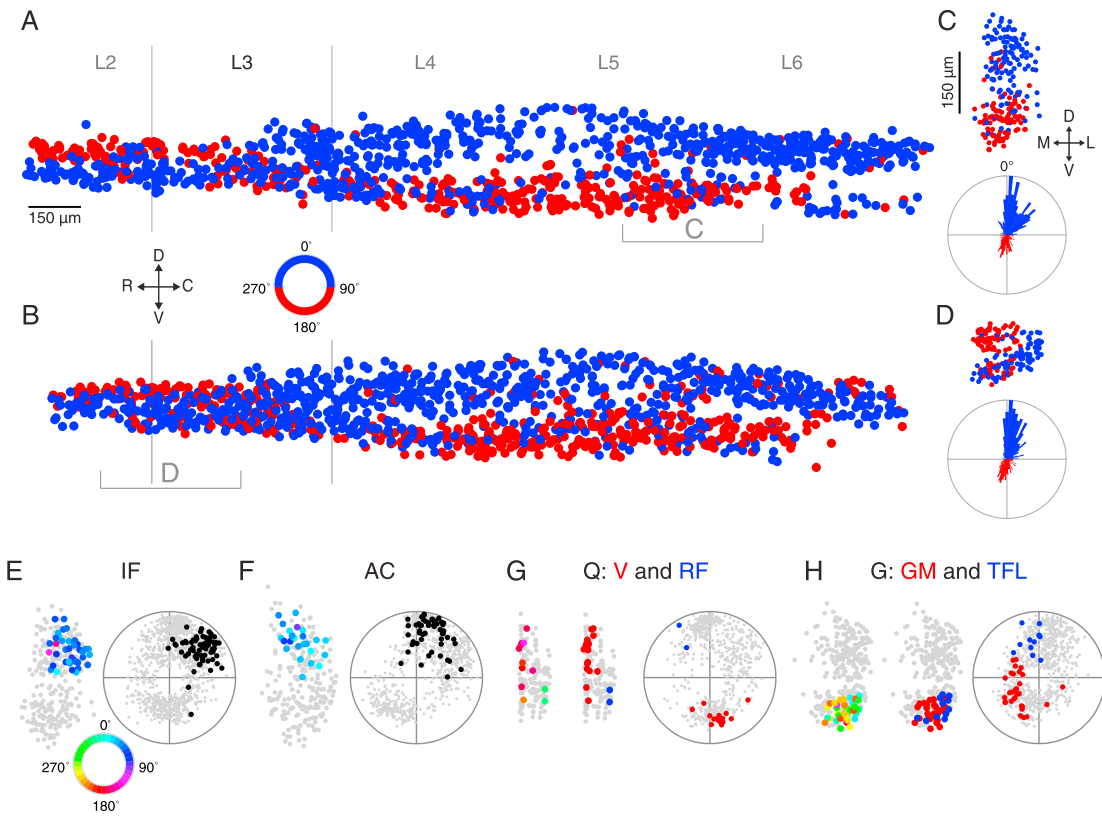


Figure S4. Spatial Analysis of Motor Neuron Phase Tuning, Related to Figure 2

(A–D) Maps of motor neuron activity matching the format and data from Figures 2A–2J, but with phase tuning represented using only two colors: blue = tuning closer to 0° and red = tuning closer to 180°.

(E–H) Transverse projections (left) from rostrocaudal segments of individual spinal cords with the phase tuning of CTB-labeled intrinsic foot (IF; E), anterior crural (AC; F), quadriceps (V/RF; G), and gluteal (GM/TFL; H) motor neurons indicated in color. For each cord, polar plots (right) show the phase tuning of all motor neurons (gray), and all IF (E), AC (F), Q (G), and G (H) motor neurons identified by CTB-labeling (black). The radial position of each point represents the circular spread around the phase tuning. Middle subplots in L and M are similar to the adjacent transverse projections, except CTB-labeled neurons are color coded red and blue according to their assignment via k-means clustering into one of two groups: vastus (V) and rectus femoris (RF) in (G), gluteus (GM) and tensor fasciae latae (TFL) in (H).

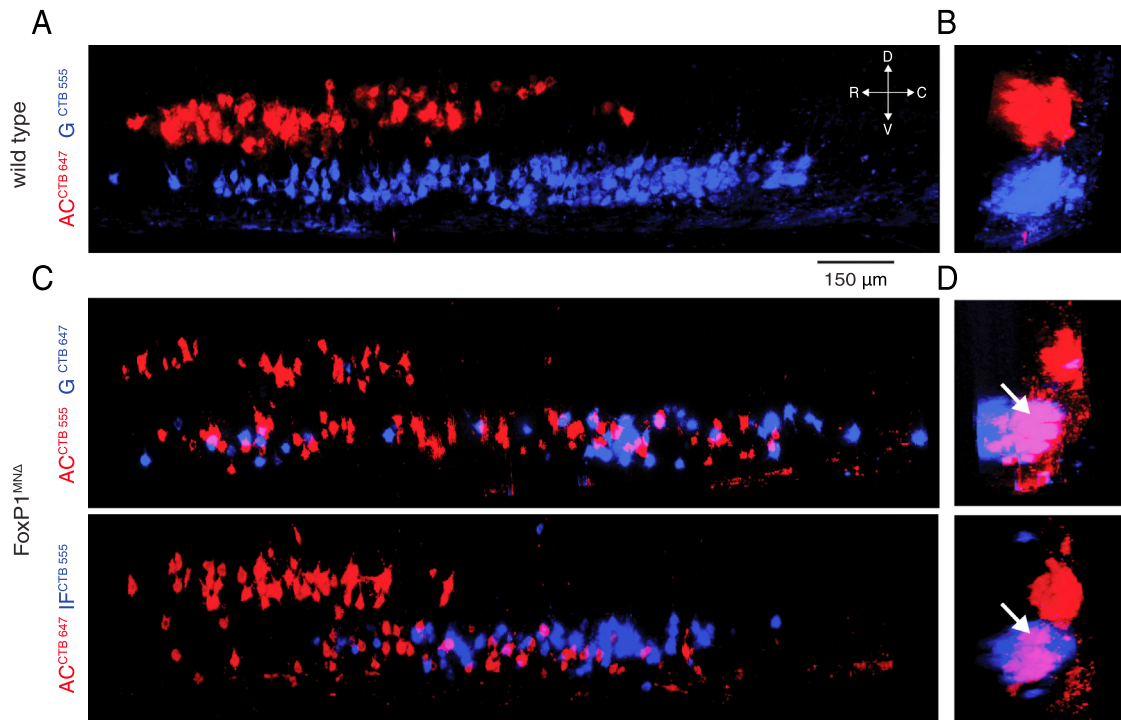


Figure S5. Spatial Organization of CTB-Labeled FoxP1^{MNA} Motor Neurons, Related to Figure 5

(A) Maximum intensity projection across a sagittally oriented lumbar spinal cord image stack from a wild-type mouse. Identified anterior crural (AC) motor neurons (red) are confined to a dorsal band above identified gluteal (G) motor neurons (blue).

(B) Transverse projection across the stack used in (A).

(C and D) Maximum intensity projections across two sagittal image stacks from two different FoxP1^{MNA} mice showing labeled AC, G, and intrinsic foot (IF) motor neurons. Arrows in (D) denote ventrally positioned AC motor neurons.

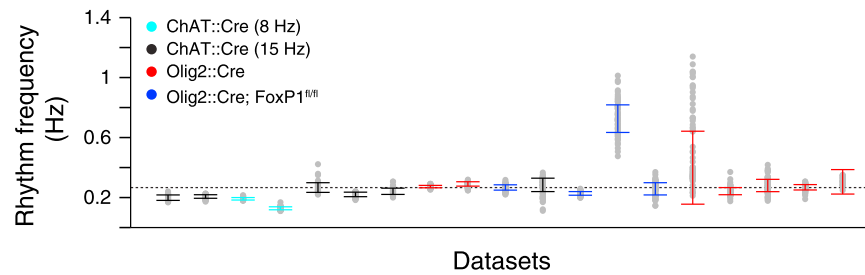


Figure S6. Consistency of Burst Frequency across Preparations, Related to Figure 5

Average burst frequency during agonist-induced locomotor firing is shown for each preparation. Dots are median frequency values derived from single image sequences. Bars denote medians \pm median absolute deviations across all image sequences from a single preparation. For wild-type preparations, mean burst frequency across all preparations = 0.25 Hz, SD = 0.062 Hz, n = 15 spinal cords. In FoxP1^{MNA} preparations, mean = 0.37 Hz, SD = 0.24 Hz, n = 4 spinal cords. Burst frequency distributions from wild-type and FoxP1^{MNA} preparations were statistically indistinguishable ($p = 0.66$, Wilcoxon rank sum test).

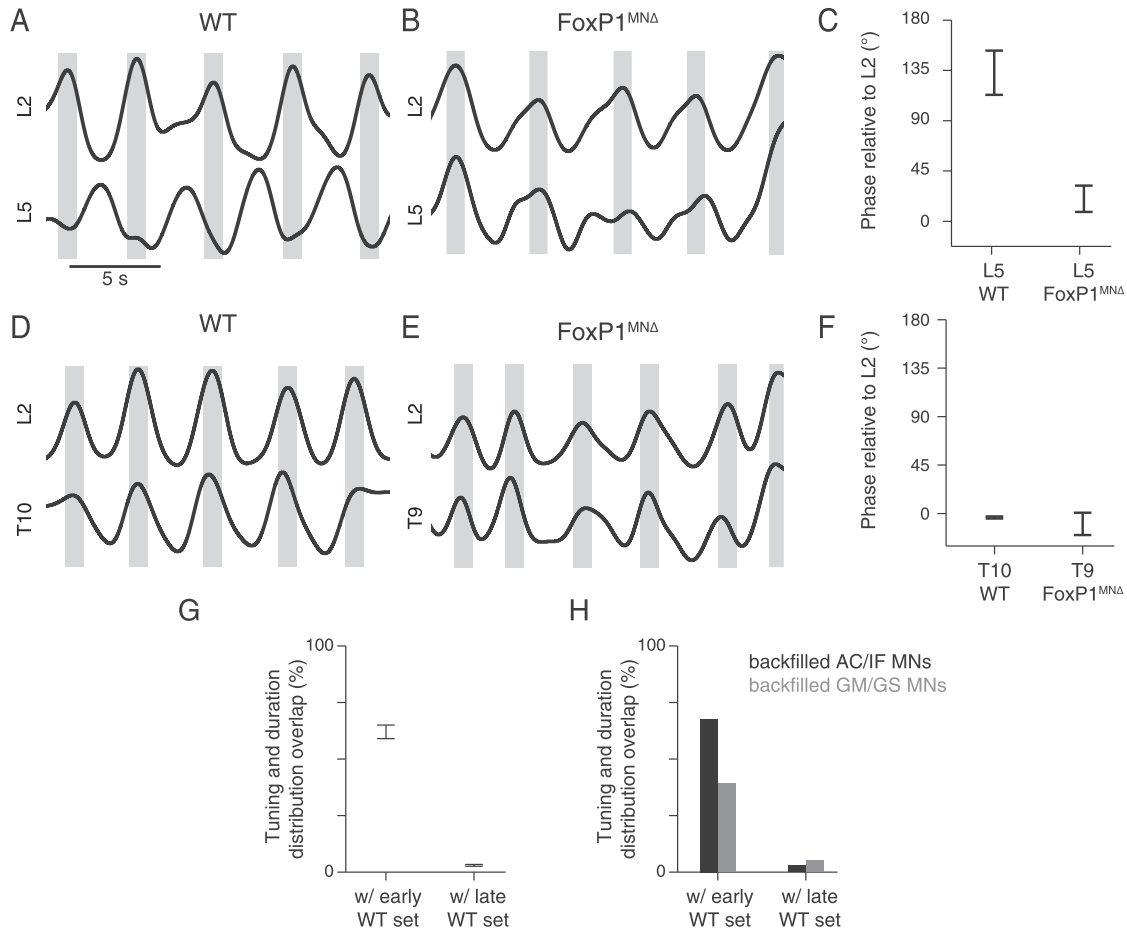


Figure S7. Comparisons between Wild-Type and FoxP1 MNA Ventral Root and Motor Neuron Activity, Related to Figure 6

(A, B, D, and E) Filtered ventral root recordings from wild-type (A,D) and FoxP1 MNA mutant mice (B,E).

(C) Phase differences between ventral root peaks measured between L5 and ipsilateral L2. Error bars represent the means \pm SEM. computed for 45 90 s recordings from a wild-type mouse (left) and 24 recordings from a FoxP1 MNA mouse (right).

(F) Phase differences between ventral root peaks measured between thoracic segments and ipsilateral L2. Error bars represent the means \pm SEM. computed for 16 90 s recordings from a wild-type mouse (left) and 28 recordings from a FoxP1 MNA mouse (right).

(G) Overlap between the joint phase tuning and burst duration distributions for motor neurons from each FoxP1 MNA cord ($n = 4$) and either the early or late firing sets of motor neurons aggregated from all wild-type cords. This was computed in order to measure the similarity in firing between FoxP1 MNA motor neurons and wild-type motor neurons assigned to either set. Overlap with the early firing wild-type set ($62 \pm 3\%$) was significantly larger than with the late firing wild-type set ($3 \pm 0.4\%$; $p = 9.1 \times 10^{-5}$, one-tailed paired t test).

(H) Overlap between the joint phase tuning and burst duration distributions for CTB-labeled FoxP1 MNA motor neurons aggregated from all 4 cords and either the early or late firing sets of motor neurons aggregated from all wild-type cords. Distributions for CTB-labeled FoxP1 MNA motor neurons overlapped much more heavily with the distribution for the early firing wild-type set (AC and IF overlap = 71%, GM and GS = 43%) than with that of the late firing wild-type set (AC and IF = 3%, GM and GS = 5%; $p = 10^{-5}$ Monte Carlo test).

Cell

Supplemental Information

Primacy of Flexor Locomotor Pattern Revealed by Ancestral Reversion of Motor Neuron Identity

**Timothy A. Machado, Eftychios Pnevmatikakis, Liam Paninski, Thomas M. Jessell, and
Andrew Miri**

Supplemental Experimental Procedures

Retrograde labeling of motor neurons

Motor neurons were retrogradely labeled *in vivo* at P1-P3 via intramuscular injections of cholera toxin B subunit conjugated to Alexa⁵⁵⁵ or Alexa⁶⁴⁷ (CTB; Life Technologies). CTB-Alexa⁵⁵⁵ and CTB-Alexa⁶⁴⁷ were used (0.1% w/v in PBS) to label up to two different muscle groups in the same mouse. Imaging experiments were conducted 24-48 h after tracer injection. Injected hindlimbs were dissected under fluorescence guidance after each experiment to verify that the diffusion of injected CTB conjugate was restricted to the targeted muscle group.

Spinal cord isolation

Mice were rapidly decapitated and the vertebral column was removed and pinned ventral side up in a Sylgard-lined (Dow Corning) dissection dish perfused with ACSF (125 mM NaCl, 25 mM NaHCO₃, 1.25 mM NaH₂PO₄, 2.5 mM KCl, 2 mM CaCl₂, 1 mM MgCl₂, and 25 mM D-glucose, 315 mOsm, equilibrated with 95% O₂ and 5% CO₂) held at 4° C with a feedback control system (ECO RE 415 S, Lauda) that cooled a brass holder encircling the dissection dish (G. Johnson, Columbia University). A ventral laminectomy was performed and dorsal and ventral roots were disconnected from their respective dorsal root ganglia and surrounding connective tissue. The isolated spinal cord was then transferred to a custom recording chamber mounted under a two-photon microscope and allowed to equilibrate for at least 30 minutes. The temperature of the ACSF in the recording chamber was held constant at 24-25° C using an inline heater (Warner). ACSF was recirculated throughout the experiment using a peristaltic pump (Gilson) with a flow rate of 9-10 mL/min.

Ventral root recording and stimulation

After equilibration, spinal cords were pinned with the left lateral side positioned upwards. Suction electrodes were mounted on custom miniature manipulators that attached to the edges of the recording chamber. These electrodes were positioned around ventral roots L1 or L2 and L4 or L5 on both the left and right sides of the cord. Additional suction electrodes used for stimulation were placed on dorsal roots L4 or L5. By stimulating dorsal roots at different intensities (8-20 μA), we were able to evoke monosynaptic responses (assessed based on

latency) between homonymous pairs of dorsal and ventral roots as well as longer latency polysynaptic responses between heteronymous pairs of roots (Mentis et al., 2011). These measurements were used to verify that electrodes were positioned correctly on the relevant roots and that we could resolve signals from each one. Electrodes were also positioned on ventral roots L3 or L4 for antidromic motor neuron stimulation. Collectively, these electrodes served to stabilize the preparation mechanically, minimizing flow-induced motion artifacts during imaging. Ventral root activity was recorded (DC-4 kHz) using a multichannel amplifier and signal conditioner (CyberAmp 380, Molecular Devices), digitized at 10 kHz (Digidata 1440A, Molecular Devices), and recorded in Clampex (v. 10.3, Molecular Devices).

Two-photon microscopy

We used a Prairie Technologies Ultima microscope constructed using an Olympus BX-51 chassis. A 20x objective (1.0 numerical aperture, 2 mm working distance; XLUMPLFLN, Olympus) was used to acquire all fluorescence images (256x256 pixels/frame). Excitation light was controlled with an electro-optical modulator (Model 302 RM, Con-Optics). We used a Chameleon Ultra II laser (Coherent) tuned to 940 nm to excite GCaMP3 and CTB-Alexa⁵⁵⁵, separated emitted fluorescence with a 560 nm dichroic (Chroma), and collected through separate emission filters (525/50 for GCaMP3 and 595/50 for CTB-Alexa⁵⁵⁵). CTB-Alexa⁶⁴⁷ was excited at 780 nm, and its fluorescence was separated with a 640 nm dichroic (Chroma) and collected through a 660/40 emission filter (Chroma). In 17 of 19 preparations, excitation light was raster scanned across the preparation at 60 Hz using a resonant galvanometer. These signals were downsampled to 15 Hz to increase the signal-to-noise ratio. In 2 of 19 preparations, the laser was scanned at 8 Hz with conventional 6 mm galvanometers in a spiral trajectory. We detected fluorescence using two non-descanned multi-Alkali photomultiplier tubes (Hamamatsu R3896, used for CTB-Alexa⁵⁵⁵ and CTB-Alexa⁶⁴⁷ imaging) and one GaAsP detector (Hamamatsu 7422PA-40, used for GCaMP3 imaging). We delivered 100-200 mW (at 940 nm excitation) and 100-300 mW (at 780 nm) to the back aperture of the objective during image acquisition.

At the beginning of each experiment, ventral root L3 or L4 was stimulated via a suction electrode to activate motor neurons antidromically (Bonnot et al., 2005; Lev-Tov and O'Donovan, 1995). Using square pulses (0.2 ms duration), we drove motor neurons to fire in a

rhythmic pattern that resembled activity observed during agonist-induced locomotor firing (Cazalets et al., 1996; Hochman and Schmidt, 1998). The antidromic stimulus consisted of ten 1.5 s long bursts, where each burst consisted of 9-25 pulses. These burst stimuli were delivered at a frequency of 0.22 Hz, approximating the 0.25 Hz average burst frequency we observed during agonist-induced locomotor firing (Figure S6). An identical stimulus waveform was used in every experiment. Stimulus intensity was 60 μ A, approximately 5 times greater than the minimum intensity needed to evoke an antidromic response (cf. Bonnot et al., 2005). This supramaximal stimulus intensity was chosen to yield a maximal number of responsive neurons, such that larger stimulation intensities would not recruit more neurons or change the observed pattern of antidromic activation. The region containing responsive motor neurons was first identified through the BX-51 epifluorescence path using a 4x Olympus objective (UPlanFL, 0.13 numerical aperture) and an EM-CCD (Hamamatsu C9100-13; 30 ms exposure per frame). We then acquired two-photon image sequences from 4-8 imaging fields within this region during stimulation.

The membrane voltage of motor neurons during antidromic stimulation in a nearly identical experimental preparation, together with earlier intracellular recordings from motor neurons, suggest that motor neurons reliably spike following each antidromic stimulation pulse when stimulated at suprathreshold intensities (G.Z. Mantis, personal communication; Bonnot et al., 2005; Brock et al., 1952). In rare instances, individual antidromic pulses sometimes induce multiple spikes, but there is no indication that the overall shape of induced bursts during antidromic stimulation would be, on average, biased such that our validation procedure would errantly validate our phase tuning estimation methods. Furthermore, our observation of phase stability over time across hundreds of motor neurons suggests that even if some bias were to exist in our phase tuning measurements, it is at least consistent over time.

After optically recording antidromic responses, we applied a rhythmogenic agonist cocktail (5 μ M NMDA, 10 μ M 5-HT, 50 μ M DA) to induce locomotor firing. One hour after application, we began acquiring image sequences in fields collectively spanning the three-dimensional extent of the lateral motor column within the mediolateral depth imageable in our preparation. To choose these imaging fields, we first manually chose 6-8 overlapping fields that

collectively spanned 2370-3330 μm along the rostrocaudal axis of the lumbar spinal cord, or approximately the whole rostrocaudal extent of the LMC. Starting from the position of each of these fields, we then chose 6-8 imaging fields equally spaced across 120-140 μm along the mediolateral axis, starting at the most lateral extent of the motor column and descending medially. Imaging fields were then visited consecutively in a pseudo-random order, and image sequences were acquired from each field for 90 s. A subset of fields were imaged a second time (6-28 locations; mean = 15) to assess stability in phase tuning over time.

Image segmentation and preprocessing

Fluorescence image sequences were preprocessed in ImageJ using custom scripts. The centroid of each motor neuron soma was manually identified, and a 15 x 15 pixel (30 x 30 μm) square region of interest (ROI) centered upon each of these centroids was defined. Fluorescence from these ROIs over time (data arrays of size 15 x 15 x T time steps) were then imported into MATLAB and processed further with custom scripts. Motor neuron somata contained in ROIs were manually matched to CTB-labeled somata apparent in static images acquired under 780 nm and 940 nm excitation from the same imaging fields. All subsequent analysis described here was performed in MATLAB.

Within each square ROI, we then found a set of pixels, called the spatial filter, which corresponded to a single motor neuron soma. First, we took each data array and decomposed it using a low-rank approximate PCA method for which we specified the decomposition rank to be 5 (Rokhlin et al., 2009). We then defined the z-scores of the first decomposition component to be our initial spatial filter and thresholded the filter such that all positive pixel weights were set to be 1, and all negative weights were set to 0. Finally, we smoothed the filter (MATLAB function bwmorph using the ‘majority’ option) and decomposed it into connected components, retaining only the largest component (all other components were set to 0). If the largest component contained fewer than 5% of the total pixels in the 15x15 pixel square, which is much smaller than the average motor neuron soma area, we discarded that data array from further analysis.

The spatial filters chosen from all data arrays taken from the same image sequence were subsequently compared to determine if any pixels had been assigned to the spatial filters of

multiple neurons. Pixels that were assigned to multiple spatial filters were re-assigned to belong to only the spatial filter arising from the nearest filter centroid. Each pixel time series in the data array was then multiplied by its corresponding spatial filter weight and summed to yield a one-dimensional fluorescence time series for each soma. Fluorescence time series were scaled to be between zero and one (for use with our spike inference algorithm) or in terms of $\Delta F/F$ for plotting. $\Delta F/F$ was defined as $(F - F_0)/F_0$, where F_0 was the 10th percentile value of F . Fluorescence time series were temporally aligned with ventral root recordings using frame acquisition times extracted from the voltage drive signal to the electro-optical modulator, which were recorded in Clampex.

Spike inference

We used new model-based fluorescence deconvolution methods (Pnevmatikakis et al., 2014) to estimate the spike train underlying each fluorescence time series. Intracellular Ca²⁺ concentration c was approximated by a first-order autoregressive model:

$$c(t) = \gamma c(t - 1) + s(t)$$

where s is the number of spikes that the neuron fired during the t -th time bin, $t = 1, \dots, T$, and γ is related to the time constant, τ , of the Ca²⁺ indicator by $\gamma = 1 - \Delta/\tau$, where the frame rate of acquisition in Hz is defined as $1/\Delta$. Each fluorescence time series f was then modeled as:

$$f(t) = \alpha c(t) + b + \varepsilon_t, \quad \varepsilon_t \sim N(0, \sigma^2)$$

where α is a nonnegative scalar and ε represents stationary Gaussian noise. This first-order model assumes an instantaneous transient rise time because the rise time of GCaMP3 in Ai38 reporter mice is roughly the same as our 67 ms/frame image acquisition rate (Zariwala et al., 2012). The baseline signal amplitude, b , was estimated by taking the 10th percentile value of each fluorescence time series and was not optimized further by the spike inference algorithm. This approach worked well with our data, because each motor neuron was active for a large fraction of its fluorescence time series.

To estimate τ , we used image sequences collected during antidromic stimulation. We assumed that the binned spike train, s , underlying each fluorescence time series, f , could be approximated by the antidromic stimulus. Using this assumption, both the s and f are known. We then estimated a single τ for each antidromic image sequence using the fluorescence time series from all responsive motor neurons within it (neuron selection criteria described in Quantification

of phase estimation error below). This calculation used the Multivariate Output-Error State-sPace (MOESP) systems identification method (Verhaegen and Verdult, 2007) implemented in the n4sid function in the MATLAB System Identification Toolbox. The median τ across all antidromic image sequences collected from a given cord was used as τ for spike inference from motor neurons from that cord. τ varied as a function of Cre driver strain used and ranged from 0.67 – 1.10 seconds (Figure S2F).

Next, we estimated the noise power σ^2 by assuming that the autocovariance function of each fluorescence signal f at lag t , $C_f(t)$, satisfies the following equation:

$$C_f(1) = \gamma C_f(0) - \sigma^2 \gamma$$

While this equality is only strictly true when neuronal spiking follows Poisson statistics, we were able to use our antidromic data to verify that this approach is approximately correct for our data (σ^2 was computed directly from each residual error distribution shown in Figure S2E, and these values match those estimated using the above equation).

Given these parameter estimates for γ and σ^2 , we then employed a constrained nonnegative deconvolution algorithm (Pnevmatikakis et al., 2014) that inferred the most likely c and s underlying each fluorescence time series:

$$\underset{c,s}{\text{minimize}} \quad \mathbf{1}_T^T s,$$

$$\text{subject to: } s \geq 0, \quad s(t) = c(t) - \gamma c(t-1), \quad \|f - c - b\mathbf{1}_T\| \leq \sigma\sqrt{T}$$

In order to find the most likely sparse spiking pattern that is sufficient to explain each fluorescence trace without overfitting, the convex program above was solved using the CVX computational package (Grant et al., 2008) or a nonnegative least angle regression algorithm (Pnevmatikakis et al., 2014). The runtime of both algorithms increased linearly with the number of time steps in the fluorescence data. The magnitude of s at each time step represents a relative estimate of number of spikes that occurred during each imaging frame. Each s value was then normalized by the maximum s for each neuron.

We also used our spike inference algorithm to estimate the signal-to-noise ratio (SNR) for each neuron in our dataset (as shown in Figure S3A-C). This quantity was defined as:

$$10 \log_{10} \left(\frac{\|c\|^2}{\sigma^2 T} \right)$$

Our spike inference algorithm yielded spike histograms consisting of a sequence of numbers between zero and one, each proportional to an estimate of neuronal firing rate at a given imaging frame. A more accurate, but less efficient, spike inference method returns continuously valued spike times, permitting the temporal pattern of multiple spikes within individual imaging frames to be detected and also providing uncertainty estimates (i.e. error bars) for all model parameters and spike inference output (Pnevmatikakis et al., 2013). In order to test whether the simpler algorithm that we used in the analysis presented in this paper errantly biased our conclusions, fluorescence data from two preparations were additionally analyzed with a different spike inference algorithm that used this more complex algorithm. We found that both methods yielded quantitatively similar results.

Validating the use of a linear model of Ca²⁺ dynamics

To test whether the linear model used to relate c to s defined in the previous section was adequate for spike inference (Figure S1D-E), we tested whether fluorescence may be better described as a nonlinear function of c :

$$n(t) = \frac{1}{1 + \exp(-\beta_0 - \beta_1 c(t))}$$

so that observed fluorescence is now given by:

$$f(t) = \alpha n(t) + b + \varepsilon_t$$

where α , b and ε are defined as in the linear model (described in the previous section). Such a model can account for nonlinearity, such as that produced by the saturation of Ca²⁺ indicator binding.

We compared the ability of these two models to predict the structure of actual fluorescence data acquired during antidromic stimulation. Model parameters underlying the sigmoidal nonlinearity (β_0 , β_1) and for scaling the data (α , b) could be directly computed in this setting because the relationship between actual spiking and fluorescence was known. For a given

set of antidromic spike times $[a_1, a_2, \dots, a_K]$, we created the binned spike train s by assigning each spike time to a correct bin and scaling it depending on how close it was to the end of the bin:

$$s(t) = \sum_{i:a_i \in [(t-1)\Delta, t\Delta]}_{i=1, \dots, K} \exp\left(-\frac{t\Delta - a_i}{\tau}\right)$$

where $\tau = -\Delta/(\gamma - 1)$ and γ was derived using the system identification approach described in the previous section.

We then computed c (termed the linear prediction in this context) given the binned antidromic stimulus, s , and the linear relationship between c and s described earlier. To generate the nonlinear prediction, we first computed the parameters $(\beta_0, \beta_1, \alpha, b)$ underlying the maximum likelihood nonlinearity by solving:

$$\min_{\beta_0, \beta_1, \alpha, b} \sum_{t=1}^T (f(t) - n(t))^2$$

With these parameters, we were able to use the binned antidromic stimulus, s , and the relationship between n and s to produce our nonlinear prediction of fluorescence data during the spike train s .

To assess the goodness of fit of each model, we computed the Pearson correlation between each the each model prediction and our fluorescence data recorded during antidromic stimulation, f , termed $\text{corr}(\text{linear prediction}, f)$ and $\text{corr}(\text{nonlinear prediction}, f)$. In nearly all cases, the difference between the models $\text{corr}(\text{nonlinear prediction}, f) - \text{corr}(\text{linear prediction}, f)$ was close to zero, suggesting the sufficiency of the linear model for use in spike inference (Figure S1D-E).

Ventral root burst identification and phase estimation

Raw ventral root recordings were first symmetrically band-pass filtered (1 Hz-1 kHz). To make root activity peaks clearer, we filtered each resulting time series $s(t)$ by replacing its value at each time step with the standard deviation of $s(t)$ from 5 ms prior to 5 ms after that time step, and ignoring the first and last 5 ms of the time series (Ahrens et al., 2012). Finally, we convolved the result with a Gaussian kernel ($\sigma = 0.5$ s) to eliminate most local maxima and thus permit reliable

peak detection. Locomotor cycles were defined as the epochs between adjacent L1 or L2 peaks. Angle gradations (0° - 360°) were uniformly distributed within each cycle. Little variation was observed between datasets referenced to L1 recordings and those referenced to L2 recordings, consistent with previous observations (Falgairolle and Cazalets, 2007; Kwan et al., 2009). Circular statistics on phase measurements were implemented using the Circular Statistics toolbox (Berens, 2009; Zar, 1999).

To quantify burst firing phase, each nonzero spike count value was assigned to a cycle phase based on its relative proximity to the root peaks immediately surrounding it (i.e. the locomotor cycle in which it fell). For each motor neuron, the circular mean of these phase values, weighted by the corresponding size of each inferred spike count, was computed at each locomotor cycle. Spikes arising from locomotor cycles that were greater than 10 s long or less than 2.5 s long (approximately 0.5x and 2.0x the average locomotor burst frequency, respectively) were excluded from the phase computation, as burst cycles of those lengths tended to arise from rare failures in peak detection or transient interruptions in rhythmic network activity. A motor neuron's phase tuning was defined as the median of the resulting values, which approximated the average phase of burst firing. We chose to quantify mean burst phase instead of onset or offset, after evaluating each statistic for all identified ankle flexor motor neurons recorded during locomotor firing and finding that the variance across the population was slightly higher for both onset and offset.

The mean burst frequency of the locomotor rhythm was quantified for each imaging field by computing the inter-burst interval time between adjacent L1 or L2 peaks and taking the inverse of these mean inter-burst interval times. The average frequency for each preparation was quantified by taking the median across all recordings.

Quantification of phase estimation error

Inferred spiking calculated from fluorescence collected during four of the ten bursts in the antidromic stimulus (Figure S2C) was used to measure the error of phase tuning estimates. These four bursts, which consisted of 16-24 pulses over 1.5 seconds, equating to an average pulse rate of 10-17 Hz, were chosen because the observed fluorescence responses well approximated those

seen during agonist-induced locomotor firing. We analyzed only those motor neurons imaged during antidromic stimulation that had a summed squared residual error value below an empirically determined threshold set such that only neurons unambiguously responding to the stimulus were included ($n = 9 - 98$ neurons per cord, mean = 26 neurons per cord, 367 neurons total; $N = 14$ spinal cords). The summed squared residual error was computed for each neuron by subtracting the normalized fluorescence data from the convolution of the antidromic stimulus underlying the fluorescence data (binned into a histogram with the bin width equal to the imaging frame rate) with an exponentially decaying kernel, $k(t) = e^{-t/\tau}$, where τ was estimated using our system identification approach described above.

We computed the phase tuning of each qualifying neuron following the same procedure used for neurons recorded during locomotor firing, except here the midpoint of each antidromic stimulus burst was defined as 0° in each cycle. Since the antidromic stimulus was assumed to be equal to the motor neuron spike train, in addition to being a phase reference the midpoint of each antidromic burst is also the true phase for each cell. The estimated phase tuning values here thus represent the errors associated with estimating phase from fluorescence.

We compared the phase tuning error distributions obtained from the use of our spike inference method to those obtained from a simpler method, termed peak detection (Figure S2G,H). In our peak detection algorithm, we symmetrically band-pass filtered the fluorescence data from 0.1 Hz to 1 Hz with a 4th order Butterworth filter, and then found the maxima of the filtered time series using the `findpeaks` MATLAB function with a minimum peak height of 0.2 times the standard deviation of the filtered time series. We also used the mean difference of the phase tuning error distributions to derive a baseline value for assessing the stability of phase tuning over time. This mean difference represents the expected difference between phase tuning measurements taken at different time points under the assumption that phase tuning does not change. The mean difference was estimated by taking $2/\sqrt{\pi}$ times the standard deviation of the observed antidromic error in each dataset.

Generation of spatial maps of phase tuning

A subset of all imaged motor neurons were included in the spatial maps of phase tuning. Neurons were selected by performing Rayleigh's test of circular uniformity on the normalized spike histogram of each neuron. Motor neurons yielding p-values ≥ 0.5 were excluded, effectively eliminating the noisiest neurons while retaining broadly tuned cells with weak signals but reliable phase tuning estimates. As imaging fields were partially overlapping, individual neurons were sometimes found in multiple image sequences. These duplicate neurons were located by finding pairs of neuron centroids located within 20 μm of each other, where each centroid was from an overlapping pair of imaging fields. Only one copy of each duplicate neuron was retained. Maps created from data obtained from both *Olig2::Cre* and *ChAT::Cre* expressing mice were quantitatively indistinguishable.

Since the variation in spinal cord thickness across segments caused the central canal to not lie straight, we corrected the positional coordinates of imaged neurons to compensate. We first fit a smoothing spline to the three dimensional positional coordinates of motor neurons using the fit function in MATLAB with the smoothness parameter set to 10^{-9} . Then, we used the smoothing spline to generate a new rostrocaudal coordinate for each neuron, given by the distance from the origin to the neuron's original rostrocaudal position as measured along the smoothing spline. The mediolateral and dorsoventral coordinates were also re-centered around the fitted smoothing spline by subtracting off the position of the smoothing spline in the original coordinate space from each original mediolateral and dorsoventral neuronal position.

To functionally identify the boundaries of certain spinal segments in these maps, epifluorescence image sequence data acquired during antidromic stimulation (4x magnification) were used. For each pixel in the imaging field, we computed the standard deviation of fluorescence across time and overlaid resulting values on their corresponding positions within epifluorescence images showing CTB-labeled cells. The resulting image showed the region of the lumbar spinal cord that had high standard deviation values indicating that it was responsive to the antidromic stimulus. We manually registered this image to our large-scale spatial maps of phase tuning by using the rostrocaudal position of CTB-labeled motor neurons. We then defined the boundaries of the antidromically activated segment as the rostral and caudal edges of the region containing responsive cells. In one case in which the caudal boundary was obscured by

the position of the ventral root in epifluorescence images, we used the center position of the ventral root as the caudal segmental boundary.

Phase synchronization

Phase synchronization was computed using normalized spike histograms yielding a Rayleigh test p value < 0.05 . This more stringent criterion was used to restrict our analyses to neurons whose somatic fluorescence was recorded with a high signal-to-noise ratio. Spike histograms, treated as time series vectors, were first band-pass filtered between 0.1 and 1 Hz (4th order symmetric Butterworth filter, MATLAB functions butter and filtfilt), in order to focus on the degree of synchronization at the frequency of locomotor firing (mean \pm s.d. = 0.25 ± 0.06 Hz, $n = 15$ spinal cords; Figure S6). Filtered histograms were then expressed in terms of instantaneous phase by taking their Hilbert transform (MATLAB function hilbert) and converting complex values to phase angles. The first and last tenths of the resulting instantaneous phase vectors were removed. To compute phase synchronization for a pair of N -element instantaneous phase vectors, we first computed their relative phase by subtracting them, yielding $\phi = [\phi_1 \dots \phi_N]$. Phase synchronization is then the scalar R given by (Mormann et al., 2000):

$$R = \left| \frac{1}{N} \sum_{j=1}^N e^{i\varphi_j} \right|.$$

To test for the significance of synchrony within and between synergy groups, we used a Wilcoxon test to compare phase synchrony index distributions with their equivalent calculated after circular permutation of one time series from each pair. Because cycle periods vary, circular permutation should reduce synchrony to a level approaching that expected by chance if the two time series were independent. Circular permutation was performed by picking a random element in one of the time series, removing the series of elements coming before it, and concatenating them to the end of the remaining time series. We also used the Wilcoxon test to compare phase synchrony index distributions within and between synergy groups. Here, we performed the test both with and without a control for differences in the proximity of neuron pairs within versus between synergist groups. In the controlled case, we first identified, for each pair of non-synergist motor neurons, the pair of synergist motor neurons not previously identified whose

proximity was most similar. The Wilcoxon test was then used to compare phase synchrony index distributions for non-synergist and identified synergist pairs.

Cycle-triggered firing rates

Cycle-triggered firing rates were computed for cells whose spike histograms yielded a Rayleigh test p value < 0.05. The firing rate vectors were computed by generating a 100-bin histogram of inferred spike counts according to their locomotor phase, then convolving these histograms with a Gaussian kernel ($\sigma = 4$ bins). Burst duration was measured from cycle-averaged firing rates by identifying the last histogram bin before, and first histogram bin after, the peak value at which the spike count is \leq half of the peak value. Burst duration was the fraction of the histogram's domain, expressed in degrees, between these two bins. The last and first histogram bins were considered to be adjacent, as implied by the cyclic nature of the histogram's domain.

After k -means clustering ($k = 2$) was performed on cycle-averaged firing rates, a clustering index was calculated to quantify the separation between the resulting two clusters. The clustering index was measured in terms of the phase of peak firing and burst duration measured from cycle-averaged firing rates. To compute this index, we first generated a two-element vector for each cycle-averaged firing rate in which the first element was peak phase and the second element was burst duration. We then computed the two-dimensional vector mean (centroid) for vectors assigned to each cluster, resulting in the cluster centroids $c^1 = \begin{bmatrix} c_1^1 \\ c_2^1 \end{bmatrix}$ and $c^2 = \begin{bmatrix} c_1^2 \\ c_2^2 \end{bmatrix}$. We then measured the root-mean-squared distance between all vectors and their centroid for each cluster, resulting in the cluster root-mean-squared distances r^1 and r^2 . The clustering index, CI , was defined as:

$$CI = \frac{2\sqrt{(c_1^1 - c_1^2)^2 + (c_2^1 - c_2^2)^2}}{r^1 + r^2}.$$

The overlap between joint distributions of peak phase and burst duration was measured by first estimating a kernel density function (using the MATLAB function kde2d obtained from the MathWorks file exchange) defined across a grid to describe each joint distribution. These density functions were normalized to ensure they integrated to one. The overlap of two density

functions was found by finding the lower of the two density's values at each grid point, then summing all of those lower values. Fold difference in similarity for the joint distribution of FoxP1^{MNA} motor neurons was computed by dividing its overlap with the early firing wild type set with that of the late firing wild type set. We tested for differences in overlap between CTB-labeled FoxP1^{MNA} motor neurons and early or late firing wild type clusters using a Monte Carlo approach. The joint peak phase and burst duration distributions for CTB-labeled FoxP1^{MNA} motor neurons were bootstrap resampled 100,000 times and overlap with both wild type clusters was computed each time. P values measuring overlap differences were calculated as $(1 + \# \text{ of bootstraps for which overlap with the late firing cluster was higher}) / 100,001$.

Analysis of motor pattern complexity

All cycle-triggered firing rates for neurons with Rayleigh test p values < 0.05 from each dataset were stored in matrices, denoted R, of size $100 \times n$, where n = number of neurons in the current dataset and 100 is the number of bins in our cycle-averaged firing rates. Each of these matrices was then approximately factorized using non-negative matrix factorization (using the MATLAB function nnmf; Lee and Seung, 1999). This method finds a pattern matrix P, and a weight matrix W, such that $R \approx PW$ with all entries in P (size $100 \times k$) and W (size $k \times n$) constrained to be non-negative. k defines the number of patterns to use in the decomposition.

We factorized the R matrix for each dataset using this approach with k=1-6. To guard against poor initializations for P and W leading to poor estimates, we set the ‘replicates’ option to 10, so each factorization operation was repeated that many times with the lowest-error replicate returned by the algorithm. As in (Dominici et al., 2011), variance explained in the data by the P and W matrices resulting from NMF at each k value was given by:

$$\text{Variance Explained} = 1 - \frac{SSE}{SST}$$

where:

$$SSE = \sum_{i=1}^n \sum_{j=1}^{100} \text{residual}_{i,j}^2 ; \text{residual} = R - PW;$$

$$SST = \sum_{i=1}^n \sum_{j=1}^{100} (R_{i,j} - \bar{R}_j)^2 ; \text{where } \bar{R} \text{ denotes the columnwise mean of } R$$

In addition, we performed a similar analysis using principal components analysis implemented by the MATLAB function `princomp`. The amount of variance explained by each principal component was simply returned by that function in the ‘latent’ argument.

SUPPLEMENTAL REFERENCES

- Ahrens, M.B., Li, J.M., Orger, M.B., Robson, D.N., Schier, A.F., Engert, F., and Portugues, R. (2012). Brain-wide neuronal dynamics during motor adaptation in zebrafish. *Nature* *485*, 471-477.
- Berens, P. (2009). CircStat: a MATLAB toolbox for circular statistics. *Journal of Statistical Software* *31*, 1-21.
- Bonnot, A., Mentis, G.Z., Skoch, J., and O'Donovan, M.J. (2005). Electroporation loading of calcium-sensitive dyes into the CNS. *Journal of Neurophysiology* *93*, 1793-1808.
- Brock, L., Coombs, J., and Eccles, J. (1952). The recording of potentials from motoneurones with an intracellular electrode. *Journal of physiology* *117*, 431-460.
- Cazalets, J.R., Borde, M., and Clarac, F. (1996). The synaptic drive from the spinal locomotor network to motoneurons in the newborn rat. *Journal of Neuroscience* *16*, 298-306.
- Dominici, N., Ivanenko, Y.P., Cappellini, G., d'Avella, A., Mondì, V., Cicchese, M., Fabiano, A., Silei, T., Di Paolo, A., and Giannini, C. (2011). Locomotor primitives in newborn babies and their development. *Science* *334*, 997-999.
- Falgairolle, M., and Cazalets, J.-R. (2007). Metachronal coupling between spinal neuronal networks during locomotor activity in newborn rat. *Journal of physiology* *580*, 87-102.
- Grant, M., Boyd, S., and Ye, Y. (2008). CVX: Matlab software for disciplined convex programming.
- Hochman, S., and Schmidt, B.J. (1998). Whole cell recordings of lumbar motoneurons during locomotor like activity in the in vitro neonatal rat spinal cord. *Journal of Neurophysiology* *79*, 743-752.
- Kwan, A.C., Dietz, S.B., Webb, W.W., and Harris-Warrick, R.M. (2009). Activity of Hb9 interneurons during fictive locomotion in mouse spinal cord. *Journal of Neuroscience* *29*, 11601-11613.
- Lee, D.D., and Seung, H.S. (1999). Learning the parts of objects by non-negative matrix factorization. *Nature* *401*, 788-791.
- Lev-Tov, A., and O'Donovan, M. (1995). Calcium imaging of motoneuron activity in the en-bloc spinal cord preparation of the neonatal rat. *Journal of Neurophysiology* *74*, 1324-1324.
- Mentis, G.Z., Blivis, D., Liu, W., Drobac, E., Crowder, M.E., Kong, L., Alvarez, F.J., Sumner, C.J., and O'Donovan, M.J. (2011). Early functional impairment of sensory-motor connectivity in a mouse model of spinal muscular atrophy. *Neuron* *69*, 453-467.
- Mormann, F., Lehnertz, K., David, P., and E Elger, C. (2000). Mean phase coherence as a measure for phase synchronization and its application to the EEG of epilepsy patients. *Physica D: Nonlinear Phenomena* *144*, 358-369.

Pnevmatikakis, E.A., Gao, Y., Soudry, D., Pfau, D., Lacefield, C., Poskanzer, K., Bruno, R., Yuste, R., and Paninski, L. (2014). A structured matrix factorization framework for large scale calcium imaging data analysis. arXiv preprint arXiv:14092903.

Pnevmatikakis, E.A., Merel, J., Pakman, A., and Paninski, L. (2013). Bayesian spike inference from calcium imaging data. Paper presented at: Signals, Systems and Computers, 2013 Asilomar Conference on (IEEE).

Rokhlin, V., Szlam, A., and Tygert, M. (2009). A randomized algorithm for principal component analysis. SIAM Journal on Matrix Analysis and Applications 31, 1100-1124.

Verhaegen, M., and Verdult, V. (2007). Filtering and system identification: a least squares approach (Cambridge university press).

Zar, J.H. (1999). Biostatistical analysis (Pearson Education India).

Zariwala, H.A., Borghuis, B.G., Hoogland, T.M., Madisen, L., Tian, L., De Zeeuw, C.I., Zeng, H., Looger, L.L., Svoboda, K., and Chen, T.W. (2012). A Cre-Dependent GCaMP3 Reporter Mouse for Neuronal Imaging In Vivo. Journal of Neuroscience 32, 3131-3141.